



1 A dataset of vertical profiles of O₃, HONO from the hyperspectral vertical
2 remote sensing network in China (2021-2024)
3 Tiliang Zou^{1,#}, Chengzhi Xing^{2,#,*}, Xiangguang Ji³, Shaocong Wei⁴, Wei
4 Tan², Haoran Liu³, Cheng Liu^{2,3,5,6,7,*}
5 ¹ School of Environmental Science and Optoelectronic Technology, University of Science and
6 Technology of China, Hefei 230026, China
7 ² Key Lab of Environmental Optics & Technology, Anhui Institute of Optics and Fine Mechanics,
8 Hefei Institutes of Physical Science, Chinese Academy of Sciences, Hefei, 230031, China
9 ³ Institute of Physical Science and Information Technology, Anhui University, Hefei 230601,
10 China
11 ⁴ Institute of Environment Hefei Comprehensive National Science Center, Hefei, 230031, China
12 ⁵ Department of Precision Machinery and Precision Instrumentation, University of Science and
13 Technology of China, Hefei 230026, China
14 ⁶ Center for Excellence in Regional Atmospheric Environment, Institute of Urban Environment,
15 Chinese Academy of Sciences, Xiamen 361021, China
16 ⁷ Key Laboratory of Precision Scientific Instrumentation of Anhui Higher Education Institutes,
17 University of Science and Technology of China, Hefei 230026, China
18
19 # These authors contributed equally to this work.
20 *Corresponding to: Chengzhi Xing (xingcz@aiofm.ac.cn); Cheng Liu (chliu81@ustc.edu.cn)
21



22 Abstract

23 Photolysis of HONO and O₃ in the troposphere is a primary source of OH radical
24 and a fundamental control on atmospheric oxidative capacity. Their vertical
25 distributions and diurnal evolution are therefore essential for elucidating
26 photochemical processes in the planetary boundary layer and the lower free
27 troposphere. Yet long-term, continuous observations of the vertical profiles of HONO,
28 O₃, their photolysis frequencies, and the resulting OH production rates remain
29 extremely limited, particularly at multi-regional and interannual scales. Here we
30 present vertical profile measurements of HONO and O₃ acquired by the Chinese
31 Hyperspectral Vertical Remote Sensing Network during 2021–2024. The dataset
32 comprises 22 representative sites spanning urban, suburban, plateau, and basin
33 environments, covering diverse surface and climatic regimes. Profiles extend from the
34 surface to 4 km with ~100 m vertical resolution and ~15 min temporal resolution.
35 Using the TUV model with co-retrieved aerosol and trace-gas profiles, we derive
36 photolysis frequencies of HONO and O₃ and the corresponding OH production rates,
37 P(OH)_{HONO} and P(OH)_{O₃}. The observations reveal robust regional patterns in the
38 diurnal and vertical structure of tropospheric photochemical activity. Photolysis
39 frequencies peak near local noon and generally increase with altitude from the surface
40 layer to the upper mixed layer and the lower free troposphere, whereas OH production
41 rates reach their maxima within the boundary layer and decrease with height.
42 Processed using a unified retrieval framework and rigorous quality control, this
43 dataset provides quantitative constraints on the contribution of HONO and O₃
44 photolysis to tropospheric OH, supports improved radical parameterizations in
45 chemical transport models, and enables synergistic multi-platform remote sensing
46 analyses. By delivering the first systematic, long-term vertical profiles of HONO, O₃,
47 and their OH production in China, this public dataset fills a critical observational gap
48 and offers a robust basis for investigating the spatiotemporal evolution of tropospheric
49 oxidative capacity across regions and altitude ranges, with substantial scientific
50 significance and long-term applicability. The dataset is available for free at Zenodo
51 (<https://doi.org/10.5281/zenodo.18489836>, Zou et al., 2026).

52

53 1. Introduction

54 Over the past decade, “the implementation of China’s Air Pollution Prevention
55 and Control Action Plan” (2013) and “the Three-Year Action Plan for Defending the
56 Blue Sky” (2018) has led to a marked reduction in fine particulate matter (PM_{2.5})
57 nationwide (Liu et al., 2023b; Wang et al., 2020). In contrast, ozone (O₃)—a
58 secondary pollutant and a major atmospheric oxidant—has continued to increase,
59 particularly in economically developed regions such as the Beijing–Tianjin–Hebei
60 area, the Yangtze River Delta, and the Pearl River Delta, where it has emerged as the
61 most intractable air-quality problem after PM_{2.5} (Guo et al., 2023; He et al., 2023a; Li
62 et al., 2020; Lyu et al., 2025; Zou et al., 2025). Photochemical air pollution is a
63 dominant driver of urban and regional air-quality degradation, characterized by the



64 rapid sunlight-driven accumulation of secondary species, most notably O₃ (Dewan
65 and Lakhani, 2022; Donzelli and Suarez-Varela, 2024; Sharma et al., 2025; Wang et
66 al., 2025b). Beyond being a typical secondary pollutant, O₃ is a powerful oxidant that
67 exerts substantial impacts on regional climate, ecosystems, and human health (Monks
68 et al., 2015; Sharma et al., 2025; Wang et al., 2025b; Xing et al., 2017). Nitrous acid
69 (HONO), a short-lived reactive nitrogen species, occurs at relatively low
70 concentrations but represents a major primary source of the OH radical, the key
71 “detergent” of the troposphere (Andersen et al., 2023; He et al., 2023c; Song et al.,
72 2023a; Zhang et al., 2023a). In polluted environments, photolysis of HONO can
73 account for 20–80% of total OH production, and its relative importance is particularly
74 pronounced during early morning and late afternoon, when solar elevation is low and
75 alternative OH sources are less efficient (Elshorbany et al., 2010; He et al., 2023c;
76 Zhang et al., 2023a). A quantitative understanding of the formation and transport of
77 both HONO and O₃ is therefore essential for elucidating the mechanisms of
78 tropospheric photochemical pollution and for designing effective mitigation strategies.

79 Despite extensive research on HONO and O₃, major gaps persist in observations
80 of their vertical structure and in the parameterization of key photochemical processes,
81 limiting a mechanistic understanding of photochemical air pollution (Liu et al., 2023a;
82 Wang et al., 2018, 2025c; Zhang et al., 2024; Zhu et al., 2025b). Vertical
83 measurements remain particularly sparse, and concurrent profiles of HONO and O₃
84 are largely unavailable (Garcia-Nieto et al., 2018a; Song et al., 2023a; Wang et al.,
85 2018, 2025c; Zhu et al., 2025b). China National Environmental Monitoring Center
86 (CNEMC), with more than 2,000 surface stations, provides routine measurements of
87 PM_{2.5}, NO₂, and SO₂, but generally lacks observations of key photochemical
88 precursors such as HONO and volatile organic compounds (VOCs) (Liu et al., 2023a;
89 Qu et al., 2020; Zhang et al., 2024; Zhu et al., 2025b). More fundamentally, surface
90 observations alone cannot resolve pollutant distributions within the planetary
91 boundary layer or capture variations in vertical atmospheric structure (Wang et al.,
92 2018, 2019, 2025c; Xuan et al., 2025a; Zhu et al., 2025b), and exclusive reliance on
93 near-surface data may therefore bias assessments of regional transport and
94 accumulation (Liu et al., 2023a; Wang et al., 2019, 2025c). Spaceborne sensors,
95 including MODIS, CALIPSO, TROPOMI, and OMI, provide global fields of aerosol
96 optical depth (AOD) and vertical column densities (VCDs) for selected trace gases.
97 However, their limited temporal sampling and spatial resolution preclude resolving
98 the pronounced diurnal variability and fine vertical structure of O₃ and HONO
99 (Itahashi et al., 2020; Johnson et al., 2024; Torres et al., 2020a; Wang et al., 2025a).
100 Chemical transport models (CTMs) and regional climate models (RCMs) can
101 reproduce the spatiotemporal evolution of pollutants, but their performance depends
102 critically on initial and boundary conditions, and uncertainties in vertical
103 parameterizations—such as turbulent mixing and chemical mechanisms—often lead
104 to substantial biases in simulated profiles (Chambers et al., 2019; Kim et al., 2024; Li
105 et al., 2021; Sekiya et al., 2025; Thürkow et al., 2024). Current in situ and remote-



106 sensing techniques also have intrinsic limitations. Lidar systems provide high-
107 resolution aerosol profiles but are restricted in detectable gaseous species and spatial
108 coverage (Anon, 2023; Johnson et al., 2024; Torres et al., 2020b). Aircraft and balloon
109 soundings yield detailed upper-air observations but are expensive and unsuitable for
110 sustained, long-term monitoring (Johnson et al., 2024; Sekiya et al., 2025; Wang et al.,
111 2025a; Yu et al., 2025). Tower measurements, while valuable near the surface, are
112 height-limited and cannot capture the full vertical variability across the boundary
113 layer (Chambers et al., 2019; Kim et al., 2024; Thürkow et al., 2024).

114 To address the observational limitations and scientific questions outlined above,
115 we developed a comprehensive dataset of vertical profiles of HONO, O₃, and their
116 photolysis frequencies using the Chinese Hyperspectral Vertical Remote Sensing
117 Network. The primary objective is to resolve the vertical structure of HONO and O₃
118 and to quantify the altitude-dependent production of OH radicals from their photolysis.
119 This dataset fills a critical gap in vertical observations of key photochemical species
120 over China and provides a unique basis for assessing the contribution of HONO
121 photolysis to boundary-layer OH, the vertical characteristics of O₃ formation, and the
122 role of aerosols in modulating photolysis rates. The dataset comprises measurements
123 from 22 ground-based sites across five major regions of China—North, East, South,
124 Central, and Southwest China—collected during 2021–2024. Its core products are
125 high-temporal-resolution vertical profiles of HONO and O₃ spanning 0–4 km. Public
126 release of this dataset will enable systematic investigations of the unresolved sources
127 of HONO in the boundary layer and the vertical variability in O₃ production
128 sensitivity. When combined with numerical models, the high-resolution vertical
129 information can be used to evaluate and refine photochemical mechanisms, quantify
130 the contribution of HONO photolysis to the tropospheric OH budget, and reduce
131 uncertainties in vertical parameterizations. These advances will, in turn, support
132 robust source attribution of O₃ pollution and inform the development of coordinated
133 regional control strategies for PM_{2.5} and O₃. The following sections describe the site
134 distribution, observational and retrieval methods, and the seasonal and diurnal
135 features of the HONO and O₃ vertical structures revealed by this dataset.

136

137 **2. Method**

138 **2.1 Description of the monitoring site**

139 The dataset is derived from 22 hyperspectral ground-based vertical remote
140 sensing stations distributed across five major regions of China—North, East, South,
141 Central, and Southwest China—forming an integrated network that samples a wide
142 range of representative atmospheric environments (Table 1). The sites span urban
143 cores, urban–suburban transition zones, regional background areas, coastal and land–
144 sea interaction regions, as well as plateau, mountain, and basin settings, thereby
145 providing a three-dimensional observational framework for key photochemical
146 species. In North China, stations at the Chinese Academy of Meteorological Sciences
147 (CAMS1, CAMS2) and the University of Chinese Academy of Sciences (UCAS),



148 located in and around Beijing (~100–120 m a.s.l.), characterize the heavily urbanized
149 and industrialized core of the Beijing–Tianjin–Hebei megacity cluster. The Wangdu
150 (WD) site in suburban Baoding represents regional background conditions, whereas
151 the Shijiazhuang Luancheng (SJZ_LC) site was included to better resolve pollution
152 features specific to industrial cities. The Shanxi University (SXU) site in the Taihang
153 Mountains (780 m a.s.l.) provides critical constraints on pollutant formation and
154 transport between mountainous terrain and adjacent plains. In East China, stations are
155 distributed across the Yangtze River Delta and its hinterland, covering topography
156 from coastal lowlands to inland mountains. The summit of Mount Tai (TS; 1,500 m
157 a.s.l.) offers vertical profiles under clean, high-altitude background conditions. The
158 Nanjing University of Information Science and Technology (NUIST) site represents a
159 densely populated and economically developed urban environment, while sites at
160 Huaibei Normal University (HNU), Anhui University (AHU), and Changfeng (CF) in
161 Anhui Province (30–35 m a.s.l.) capture urban–suburban transition regimes.
162 Southwest China is represented by the Chengdu Academy of Environmental Sciences
163 (CDAES; 505 m a.s.l.) on the Chengdu Plain and the Chongqing (CQ; 332 m a.s.l.)
164 site within the Sichuan Basin. These stations are strategically located to investigate
165 pollutant accumulation and transport under high-humidity conditions and strong
166 topographic confinement, and to probe photochemical processes in complex terrain.
167 In South China, a dense network was established over the Pearl River Delta megacity
168 region. In addition to sites at the Guangzhou Institute of Geochemistry (GIG) and the
169 Southern University of Science and Technology (SUST) in Shenzhen, multiple
170 stations in Guangzhou (Zhuliao, Nansha, Timian, Gongyuan, and Daxuecheng; 15–
171 155 m a.s.l.) form an intra-urban array. This configuration allows detailed
172 examination of the combined influences of land–sea breezes, anthropogenic emissions,
173 and local meteorology on the vertical distributions of HONO and O₃. Central China is
174 represented by the Luoyang (LY) site, located in the middle reaches of the Yellow
175 River within a mixed industrial–agricultural region, providing key constraints on
176 regional transport and accumulation over the central plains. Together, the broad
177 geographic coverage and pronounced contrasts in elevation and surface type make
178 this network well suited to resolve the vertical distributions of aerosols, HONO, and
179 O₃ across urban, suburban, coastal, mountainous, and basin environments. It thus
180 offers a robust observational basis for investigating the dynamics of photochemical air
181 pollution over major regions of China.

182 Table 1. Geographic information of the stations in the Chinese Hyperspectral Ground-
183 Based Vertical Remote Sensing Network.

Region	Site (code)	Longitude (° E)	Latitude (° N)	Altitude (m)
North China	Chinese Academy of Meteorological Sciences (CAMS1)	116.32	39.94	100
	Chinese Academy of Meteorological Sciences (CAMS2)	116.32	39.94	100
	University of Chinese Academy of Sciences (UCAS)	116.67	40.4	120
	Wangdu (WD)	115.15	38.17	35



	Shijiazhuang_Luancheng (SJZ_LC)	114.61	37.91	70
	Shanxi University (SXU)	112.58	37.63	780
	Taishan (TS)	117.1	36.25	1500
	Nanjing University of Information Science and Technology (NUIST)	118.71	32.2	73
East China	Lin'an (LA)	119.75	30.3	140
	Huaibei Normal University (HNU)	116.8	33.98	35
	Anhui University (AHU)	117.18	31.77	30
	Changfeng (CF)	117.18	32.21	30
	Chengdu Academy of Environmental Sciences (CDAES)	104.04	30.65	505
Southwest China	Chongqing (CQ)	106.5	29.6	332
	Guangzhou Institute of Geochemistry (GIG)	113.35	23.15	30
	Southern University of Science and Technology (SUST)	113.99	22.59	40
South China	Guangzhou_Zhuliao (GZ_ZL)	113.34	23.36	20
	Guangzhou_Nansha (GZ_NS)	113.61	22.77	15
	Guangzhou_Timian (GZ_TM)	113.29	23.55	155
	Guangzhou_Gongyuan (GZ_GY)	113.26	23.13	15
	Guangzhou_Daxuecheng (GZ_DXC)	113.39	23.04	10
Central China	Luoyang (LY)	112.45	34.67	100

184

185

2.2 Instrument setup

186

187

188

189

190

191

192

193

194

195

196

197

198

199

200

201

202

2.3 Spectral retrieval

203

204

205

206

207

208

209

Ultraviolet–visible spectra measured by the ground-based instruments were analysed with the QDOAS software developed by BIRA-IASB. Differential optical absorption spectroscopy (DOAS) was applied to retrieve the differential slant column densities (DSCDs) of the oxygen dimer (O_4), O_3 , and HONO. For each elevation scan, the zenith spectrum (90° elevation) was used as the reference and subtracted from spectra at lower elevation angles, thereby isolating the narrow-band absorption features of trace gases from broadband structures and enabling robust retrieval of

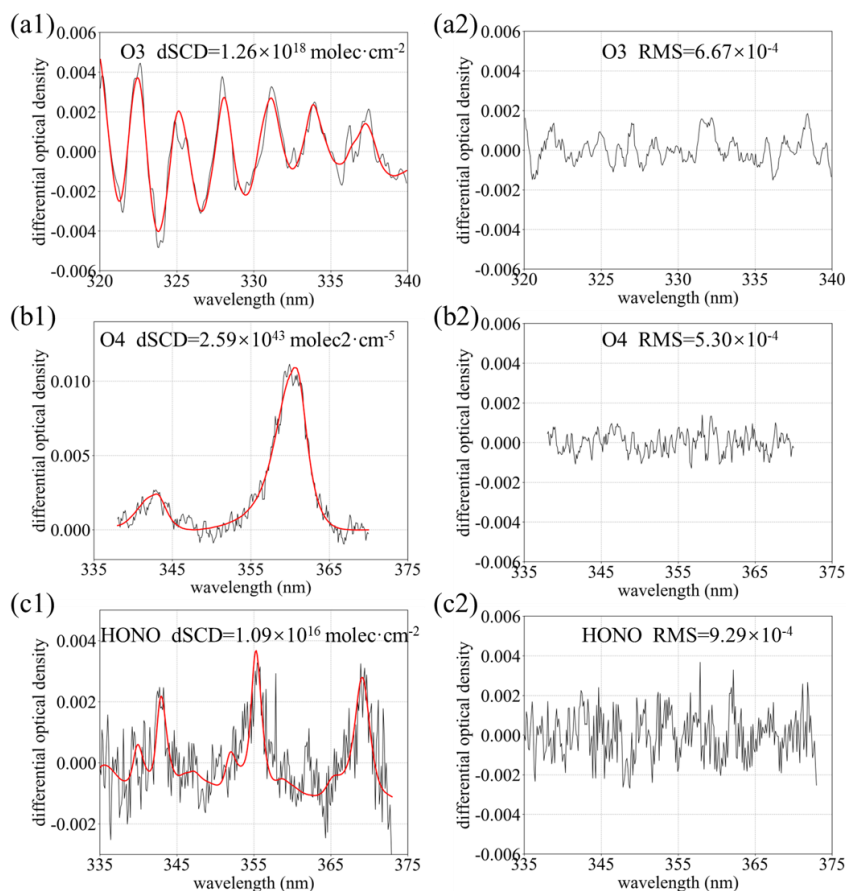


210 target species. The fitting settings follow Xing et al. (2021, 2024a, b) and are
 211 summarized in Table 2. To account for the Ring effect arising from rotational Raman
 212 scattering and Fraunhofer line filling-in, a Ring spectrum calculated with DOASIS
 213 was included in the fit. Broadband spectral structures were represented and removed
 214 using a fifth-order polynomial, allowing accurate separation of narrow-band
 215 molecular absorption. Strict quality control was applied: only retrievals with a root-
 216 mean-square (RMS) fitting residual below 1×10^{-3} were retained, ensuring the
 217 robustness and stability of the dataset. Representative spectral fits and residuals for O₄,
 218 O₃, and HONO are shown in Figure 1.

219 Table 2. Detailed retrieval settings for O₄, O₃, and HONO.

Parameter	Data source	Fitting interval		
		O ₄	O ₃	HONO
Wavelength range		338–370 nm	320–340 nm	335–373 nm
NO ₂	220 K, I ₀ * correction (SCD of 10 ¹⁷ molec·cm ⁻²); (Vandaele et al., 1998)	√	×	√
NO ₂	298 K, I ₀ correction (SCD of 10 ¹⁷ molec·cm ⁻²); (Vandaele et al., 1998)	√	√	√
O ₃	223 K, I ₀ correction (SCD of 10 ¹⁸ molec·cm ⁻²); (Serdyuchenko et al., 2014)	√	√	√
O ₃	243 K, I ₀ correction (SCD of 10 ¹⁸ molec·cm ⁻²); (Serdyuchenko et al., 2014)	×	×	√
O ₃	293 K, I ₀ correction (SCD of 10 ¹⁸ molec·cm ⁻²); (Serdyuchenko et al., 2014)	√	√	×
O ₄	293 K, I ₀ correction (SCD of 3×10 ⁴³ molec ² ·cm ⁻⁵); (Thalman and Volkamer, 2013)	√	√	√
HCHO	293 K, I ₀ correction (SCD of 5×10 ¹⁵ molec·cm ⁻²); (Orphal and Chance, 2003)	√	√	√
BrO	273 K, I ₀ correction (SCD of 10 ¹³ molec·cm ⁻²); (Fleischmann et al., 2004)	√	×	√
Ring	Ring spectra calculated with DOASIS	√	√	√
HONO	I ₀ correction (SCD of 10 ¹⁵ molec·cm ⁻²); (Stutz et al., 2000)	×	×	√
Polynomial degree		5	5	5
Intensity offset		Constant	Constant	No

220 * Solar I₀ correction, Aliwell et al.(2002).



221

222 Figure 1. (a1) O₃, (b1) O₄, and (c1) HONO DOAS fitting examples; (a2) O₃, (b2) O₄,
 223 and (c2) HONO fitting residuals.

224

225 2.4 Vertical profile retrieval algorithm

226 Vertical profiles of aerosols and trace gases (HONO and O₃) were retrieved using
 227 an inversion framework based on the optimal estimation method (OEM). The forward
 228 radiative transfer calculations were performed with the linearized pseudo-spherical
 229 vector discrete ordinate model VLIDORT (Spurr, 2006). The posterior state vector \mathbf{x}
 230 was obtained by minimizing the cost function χ^2 :

$$231 \quad \chi^2 = (\mathbf{y} - \mathbf{F}(\mathbf{x}, \mathbf{b}))^T \mathbf{S}_\varepsilon^{-1} (\mathbf{y} - \mathbf{F}(\mathbf{x}, \mathbf{b})) + (\mathbf{x} - \mathbf{x}_a)^T \mathbf{S}_a^{-1} (\mathbf{x} - \mathbf{x}_a) \quad (1)$$

232 where \mathbf{y} denotes the measured DSCDs, $\mathbf{F}(\mathbf{x}, \mathbf{b})$ is the forward model, \mathbf{b} represents
 233 ancillary meteorological parameters (e.g., temperature, pressure, single-scattering
 234 albedo, and asymmetry factor), \mathbf{x}_a is the a priori state vector, \mathbf{S}_ε is the measurement
 235 error covariance matrix, and \mathbf{S}_a is the a priori covariance matrix. For both aerosols
 236 and trace gases, the a priori vertical profiles were assumed to decrease exponentially



237 with altitude, reflecting the characteristic rapid decay of pollutant concentrations
238 within the planetary boundary layer. Because the absorption of the O₄ is strongly
239 linked to aerosol optical properties, aerosol vertical profiles were first retrieved from
240 multi-elevation O₄ DSCDs and subsequently used as inputs to the forward model for
241 the retrieval of O₃ and HONO profiles. The atmosphere from the surface to 4 km was
242 discretized into 20 layers with a vertical resolution of 200 m (Xing et al., 2024b).
243 Retrievals were subjected to strict quality control: profiles with degrees of freedom
244 (DOF) below 1.0, χ^2 values exceeding 200, or relative uncertainties greater than 50%
245 were excluded from further analysis.

246

247 **2.5 TUV model**

248 Photolysis rates of HONO and O₃ were computed with the Tropospheric
249 Ultraviolet and Visible (TUV) radiative transfer model developed by NCAR, which is
250 based on rigorous radiative transfer theory and implemented in FORTRAN
251 (<https://www2.acom.ucar.edu/modeling/tropospheric>, last access: 26 January 2026).
252 The TUV model simulates the propagation of solar radiation in the troposphere under
253 prescribed optical and chemical conditions and provides spectrally resolved
254 photolysis frequencies for key atmospheric reactions. These rates were used to
255 quantify the contributions of HONO and O₃ photolysis to OH production. Model
256 inputs included AOD at ~361 nm derived from MAX-DOAS-retrieved aerosol
257 extinction profiles, total ozone column from daily TROPOMI observations (typically
258 260–280 DU), and single-scattering albedo (SSA) constrained by regression analyses
259 of O₄ absorptions at 361 and 477 nm (Xing et al., 2019).

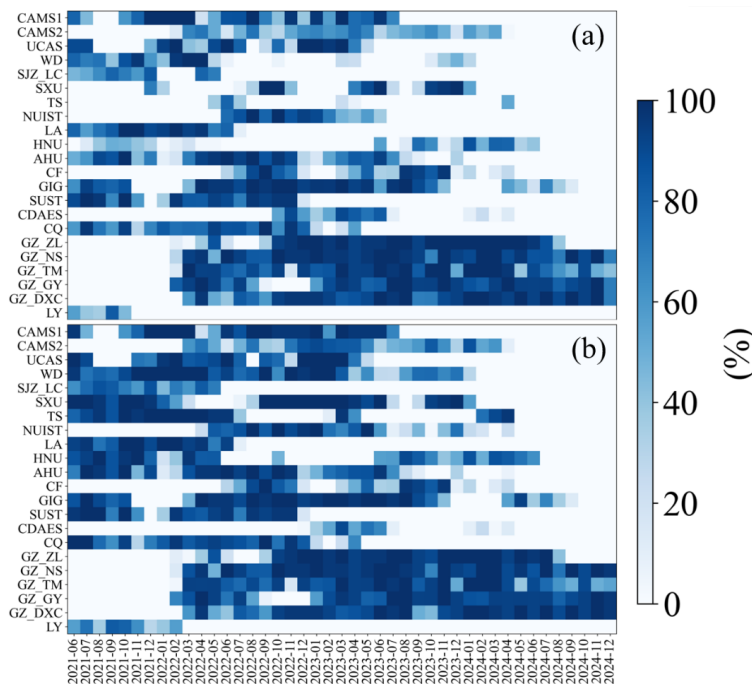
260

261 **3. Vertical profile observations of atmospheric composition**

262 Figure 2 summarizes the monthly completeness of O₃ and HONO vertical profile
263 measurements at 22 sites from 2021 to 2024. Shading denotes the fraction of valid
264 observations, with 100% indicating uninterrupted daytime measurements and
265 successful profile retrievals throughout the month. Because stations were
266 commissioned at different times and operated under varying maintenance and field
267 conditions, the available observation periods differ among sites. Most stations provide
268 long, continuous time series of both HONO and O₃. More than ~85% of the sites
269 operated for over one year, and ~60% for more than two years, demonstrating the
270 temporal stability of the network. This coverage enables robust characterization of
271 seasonal and diurnal variability under diverse climatic regimes and emission
272 backgrounds. Although a few sites had shorter operational periods owing to
273 instrument commissioning and field constraints, they still delivered several months of
274 continuous high-quality data, which are valuable for regional intercomparison and
275 support analyses of long-term trends and photochemical processes. Isolated months
276 with missing or incomplete data occur at some sites, primarily because of unavoidable
277 factors such as instrument maintenance, power interruptions, persistent cloud or
278 precipitation, and quality-control filtering (e.g., excessive fitting residuals or low DOF



279 in the retrievals).



280

281 Figure 2. Monthly data completeness of the vertical profiles of (a) O₃ and (b) HONO.

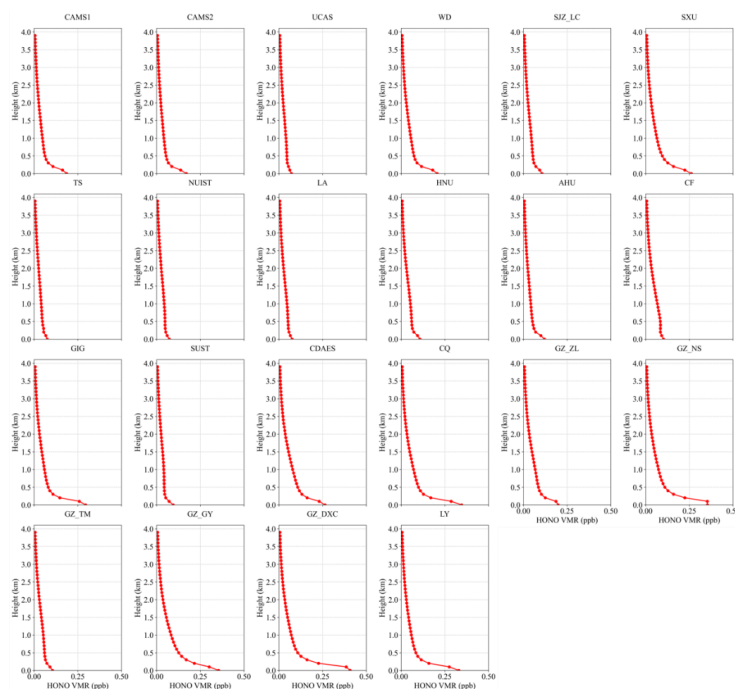
282

283 3.1 HONO

284 Figure 3 presents the 2021–2024 mean vertical profiles of HONO across all sites.
285 At every location, HONO is strongly enriched near the surface and decreases rapidly
286 with height, following an approximately exponential decay. This structure is
287 characteristic of a boundary-layer-dominated species controlled by ground-based
288 sources (Li et al., 2025b; Meng et al., 2020; Xing et al., 2024c; Xu et al., 2021). Peak
289 mixing ratios occur within the lowest 0–0.5 km, decline sharply between 0.5 and 1.5
290 km, and generally fall to regional background or near the detection limit above 2
291 km (<0.05–0.1 ppb), becoming negligible by 4 km. Such steep gradients reflect dominant
292 near-surface emissions and nocturnal heterogeneous formation of HONO from NO₂
293 on ground and aerosol surfaces, combined with its short photochemical lifetime and
294 rapid daytime photolysis, which preclude sustained accumulation in the free
295 troposphere (Li et al., 2025b; Meng et al., 2020; Xing et al., 2024a). Pronounced
296 regional contrasts are evident. Urban sites in North and East China (e.g., CAMS1,
297 CAMS2, WD, SXU, AHU) exhibit the highest near-surface HONO (0.3–0.5 ppb
298 below 0.3 km), followed by a rapid decrease to <0.1 ppb above 1 km. The sharp
299 vertical gradients and absence of secondary maxima aloft indicate strong control by
300 surface sources and nocturnal heterogeneous production, with efficient removal by
301 turbulent mixing and photolysis within the planetary boundary layer (Xu et al., 2021).



302 In contrast, background or relatively clean sites (e.g., TS, LA) show much lower
303 concentrations, with near-surface values typically <0.2 ppb and a monotonic decrease
304 with altitude, consistent with weak local emissions and dominance of regional
305 background (Garcia-Nieto et al., 2018b; Li et al., 2025b). Sites in South and
306 Southwest China (e.g., GZ_ZL, GZ_NS, GZ_DXC, CQ, CDAES) display a similar
307 monotonic decay: elevated HONO confined to the lowest 0–0.5 km and rapid
308 attenuation to background levels above 1–2 km, without a persistent mid-level
309 enhancement. Although near-surface mixing ratios at some locations (e.g., GZ_DXC,
310 CQ) approach or slightly exceed 0.3 ppb, their vertical decay rates are comparable to
311 those at northern and eastern urban sites. This indicates that, even under high
312 humidity or complex topography, HONO remains largely restricted to the lower
313 boundary layer, governed by its short lifetime, fast photolysis, and dilution by
314 convective mixing, while large-scale vertical transport contributes little to its
315 maintenance aloft (Li et al., 2025b; Xing et al., 2021b; Xu et al., 2021). Seasonal
316 mean profiles are shown in Figures S1–S4. Taken together, the regionally averaged
317 profiles consistently demonstrate strong near-surface accumulation and rapid vertical
318 attenuation of HONO. This confirms that HONO is a short-lived, boundary-layer-
319 derived reactive nitrogen species, tightly coupled to surface emissions and
320 heterogeneous chemistry. It therefore plays a key role in initiating early-morning OH
321 production and regulating boundary-layer oxidizing capacity, whereas its direct
322 impact in the free troposphere is comparatively minor.



323
324

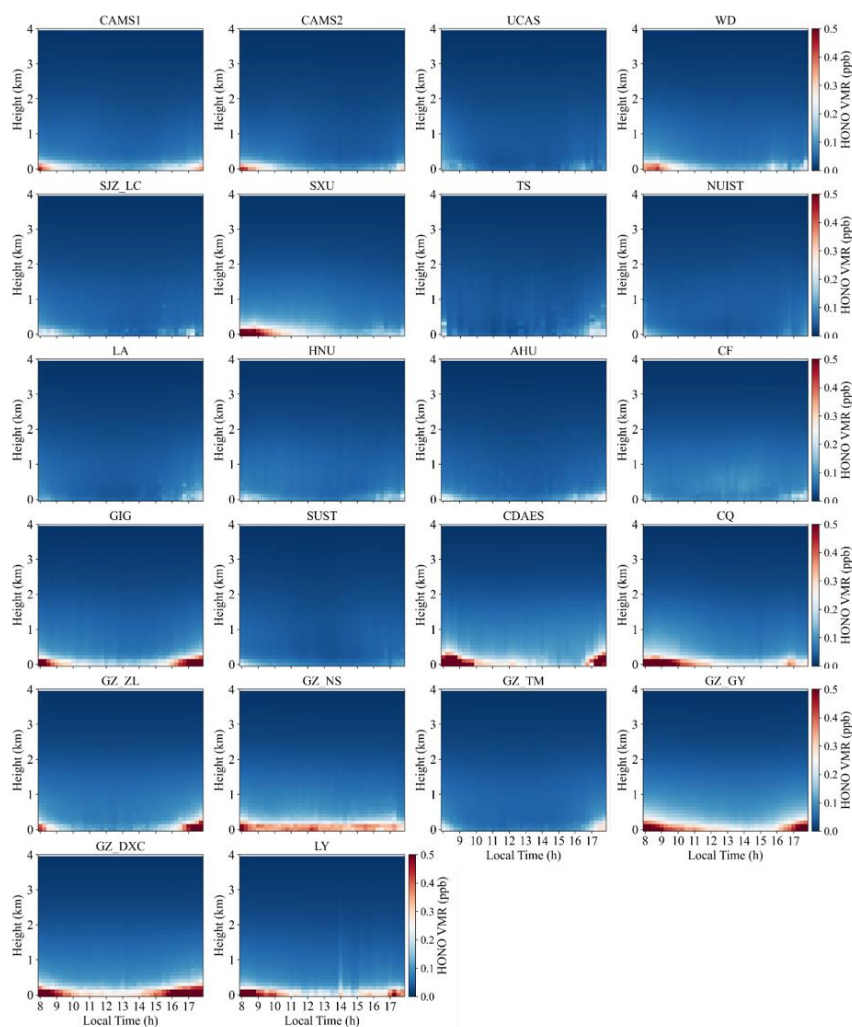
Figure 3. Mean vertical profiles of HONO averaged over 2021–2024.



325 Figure 4 illustrates the mean diurnal evolution of HONO. As a key reactive
326 nitrogen species, HONO exhibits vertical and temporal patterns that integrate the
327 effects of surface emissions, heterogeneous and photochemical processes, and
328 boundary-layer dynamics. Based on HONO data obtained from the hyperspectral
329 vertical remote-sensing network, pronounced regional and site-specific patterns are
330 observed. Across North China (CAMS1, CAMS2, UCAS, WD, SJZ_LC and SXU),
331 HONO exhibits a clear near-surface morning maximum followed by an afternoon
332 minimum. At CAMS1 and CAMS2, the 0–1 km volume mixing ratio (VMR) peaks at
333 08:00–10:00 local time (0.3–0.4 ppb) and decreases to 0.1–0.2 ppb by 14:00–16:00.
334 This pattern reflects nocturnal accumulation driven by heterogeneous conversion of
335 NO₂ on aerosol and ground surfaces (Liu et al., 2022a; Xing et al., 2023; Xuan et al.,
336 2025b), and after sunrise, enhanced solar radiation leads to the release and
337 photochemical processing of HONO; meanwhile, morning rush-hour emissions of
338 NO₂ and VOCs further promote HONO formation (Garcia-Nieto et al., 2018a; Zhang
339 et al., 2025a). At the mountain site SXU, topography-induced temperature inversions
340 enhance nighttime accumulation, yielding a more pronounced morning peak. In
341 contrast, UCAS and WD, characterized by weaker anthropogenic emissions, show
342 lower near-surface HONO levels and smaller diurnal amplitudes. In East China (TS,
343 NUIST, LA, HNU, AHU and CF), urban sites display modest morning enhancements
344 (0.2–0.3 ppb at 08:00–10:00) followed by afternoon decreases driven by boundary-
345 layer growth and photolysis. At the high-altitude TS site (1500 m), HONO remains
346 below 0.1 ppb with weak diurnal variability, reflecting clean background conditions
347 and efficient vertical mixing. Sites with dense vegetation or agricultural land use (LA
348 and CF) may receive contributions from biogenic VOC-related chemistry, but the
349 overall pattern still features a subdued morning maximum. At South China and
350 Southwest China sites (GIG, SUST, CDAES, CQ and the Guangzhou cluster: GZ_ZL,
351 GZ_NS, GZ_TM, GZ_GY and GZ_DXC), warm and humid conditions together with
352 basin or coastal circulations further modulate the diurnal cycle. Urban stations
353 typically reach 0.3–0.5 ppb near the surface in the morning and decline to 0.1–0.2 ppb
354 in the afternoon. In the Sichuan Basin (CQ), strong nocturnal inversions favour
355 HONO accumulation, producing slightly higher morning peaks (0.4–0.5 ppb). At
356 coastal sites, land–sea breeze circulation leads to a transient morning enhancement
357 followed by dilution by cleaner marine air masses. At the Central China site LY, the
358 diurnal pattern resembles that in North and South China, with a clear morning
359 maximum and lower concentrations in the afternoon associated with boundary-layer
360 development. Seasonal mean diurnal vertical profiles are shown in Figures S5–S8.
361 Overall, the diurnal cycle of HONO is governed by three coupled processes: (i)
362 nocturnal heterogeneous production from NO₂ on aerosol and surface substrates,
363 which drives early-morning maxima (Li et al., 2025b; Meng et al., 2020; Xuan et al.,
364 2024); (ii) enhancement by morning anthropogenic emissions of NO_x and VOCs from
365 traffic and industrial activities (Hao et al., 2020; Zhang et al., 2025a, 2023b); and (iii)
366 rapid photolysis and boundary-layer dilution in the afternoon (Xing et al., 2021b,



367 2024a; Zhang et al., 2023b). Regional contrasts arise from the combined effects of
368 emission intensity, topography (basin, mountain and coastal settings), and
369 meteorological conditions, particularly temperature inversions and ventilation
370 efficiency (Li et al., 2025b; Xuan et al., 2024; Zhang et al., 2025a).



371

372

373

374

3.2 O₃

375

376

377

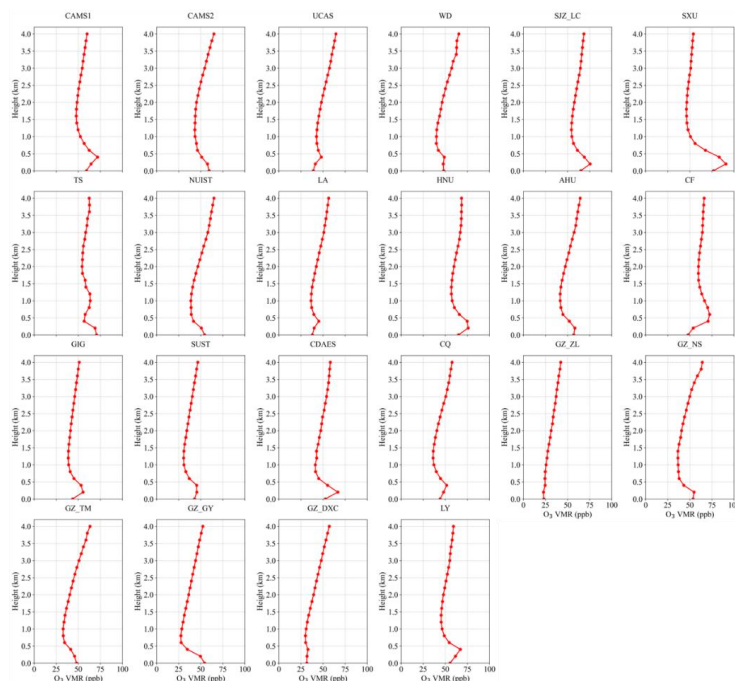
378

379

Figure 5 presents the mean vertical profiles of O₃ averaged over 2021–2024 for all sites. A consistent “low near the surface–high aloft” structure is observed, characterized by a monotonic increase or a weak S-shaped pattern. O₃ VMR are lowest in the lowest 0–0.5 km (20–60 ppb), rise rapidly between 1 and 2 km, and reach daytime maxima at 3–4 km (60–100 ppb). This vertical gradient agrees well



380 with MAX-DOAS and ozone-sonde observations over eastern China and other
381 regions worldwide (Couillard et al., 2021; Ji et al., 2023; Liao et al., 2024; Su et al.,
382 2017; Wang et al., 2018; Zeng et al., 2023), and reflects the combined effects of
383 strong near-surface NO₂ titration, dry deposition, and boundary-layer mixing that
384 suppress O₃, together with photochemical production and regional transport that
385 enhance O₃ aloft (Couillard et al., 2021; Donzelli and Suarez-Varela, 2024; Liao et al.,
386 2024; Zeng et al., 2023; Zhu et al., 2025b). Within the boundary layer (0–1 km), O₃
387 generally increases sharply with height, and a weak local maximum or inflection is
388 often found at 0.2–0.5 km. This contrasts with the vertical distributions of NO₂ and
389 HCHO at the same sites, which show high near-surface concentrations dominated by
390 emissions (Couillard et al., 2021; Hu et al., 2024; Hong et al., 2022; Jiao et al., 2025;
391 Liu et al., 2023b). In contrast, O₃ is efficiently removed near the ground by nocturnal
392 NO₂ titration and daytime surface deposition (Liao et al., 2024; Xing et al., 2022). At
393 urban and suburban stations (e.g., UCAS and CF), O₃ in the lowest 0–0.3 km can
394 decrease to 20–40 ppb, indicating strong titration by traffic and industry related NO₂
395 (Hu et al., 2024). Between 1 and 3 km, O₃ increases nearly monotonically at most
396 sites, with the largest vertical gradient typically occurring around 2–3 km. This layer
397 often corresponds to the daytime boundary-layer top or the nocturnal residual layer
398 and represents a key altitude for regional photochemical accumulation and downward
399 transport (He et al., 2023b; Liao et al., 2024; Zhu et al., 2025a). Numerous studies
400 have shown that O₃-rich air in the upper boundary layer and residual layer can be
401 mixed downward during boundary-layer growth, and that O₃ stored aloft at night is re-
402 entrained to the surface the following morning, making an important contribution to
403 surface O₃ levels (Ancellet et al., 2024; Donzelli and Suarez-Varela, 2024; Liu et al.,
404 2022b; Shi et al., 2022; Song et al., 2024; Wang et al., 2024b). At 3–4 km, O₃ VMR
405 further increase and tend to level off, with some sites exhibiting distinct maxima. At
406 these altitudes, the influence of surface NO₂ titration becomes negligible, whereas
407 long-range transport and possible stratosphere–troposphere exchange start to play a
408 role. Previous studies have shown that enhanced O₃ at 3–5 km over East Asia in
409 spring and summer can partly arise from stratospheric intrusions and westerly long-
410 range transport (Li et al., 2025a; Liao et al., 2024, 2025; Park et al., 2020). The
411 pronounced O₃ enhancements observed at 3–4 km at sites such as CQ, GZ_TM and
412 SUIST are therefore likely linked to free-tropospheric background O₃ and regional-
413 scale transport processes. Seasonal mean O₃ vertical profiles are shown in Figures
414 S9–S12.



415

416

Figure 5. Mean vertical profiles of O₃ averaged over 2021–2024.

417

418

419

420

421

422

423

424

425

426

427

428

429

430

431

432

433

434

435

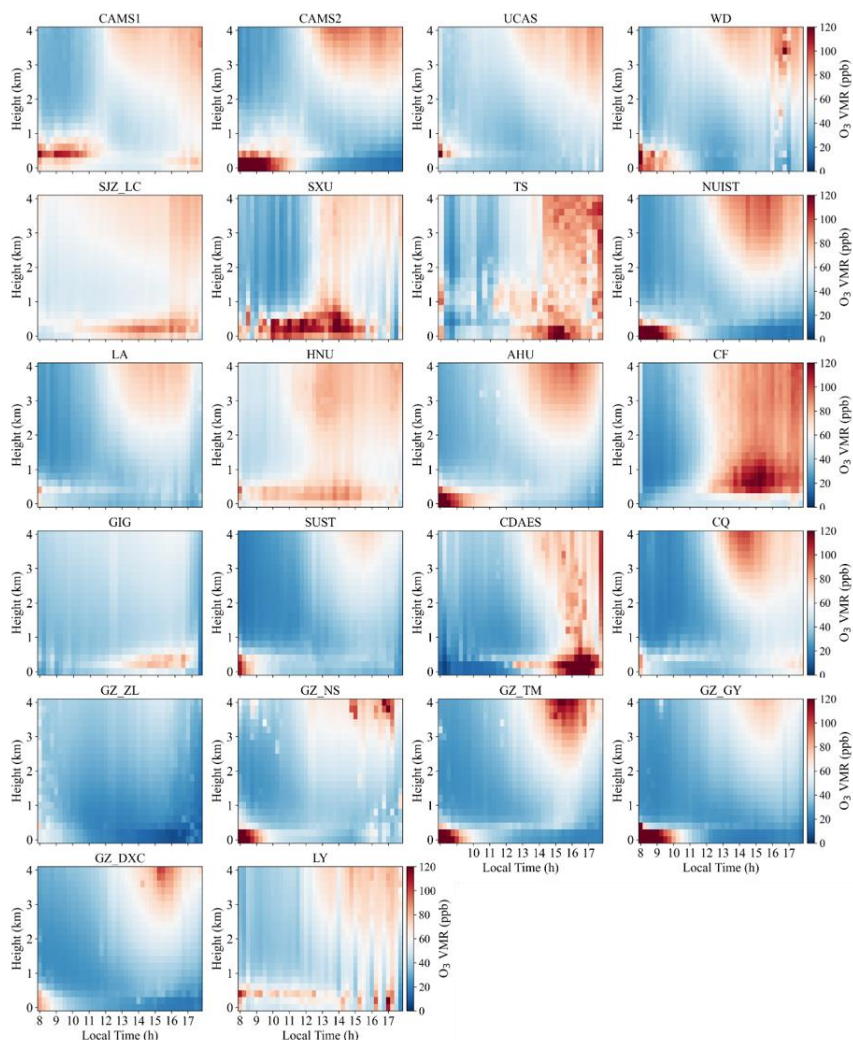
436

437

Figure 6 presents the mean diurnal evolution of O₃. All sites exhibit pronounced daily cycles with clear regional contrasts. O₃ typically peaks in the morning (08:00–10:00) or in the early afternoon (12:00–15:00), in phase with the diurnal variation of solar irradiance and photochemical reaction rates (Xia et al., 2021; Yang et al., 2020). This behaviour is most evident in North and East China, whereas the cycle is weaker in South China, likely owing to persistently high temperature and humidity that modulate boundary-layer development and photochemistry (Zhou et al., 2022). At several sites (e.g., TS, CDAES and CQ), enhanced O₃ at 1–2 km during 12:00–15:00 points to the influence of local meteorology and emission distributions (Chen et al., 2023; Li et al., 2025a). In contrast, morning maxima at CAMS1, CAMS2, UCAS, NUJST and AHU reflect the rapid re-entrainment and photochemical processing of O₃ accumulated overnight after sunrise (David and Nair, 2011; Liao et al., 2023). The vertical structure of the diurnal cycle also differs markedly among regions. North China sites show strong near-surface variability, whereas peak O₃ in South China is generally lower, consistent with regional differences in pollution levels and meteorological conditions. Relatively high near-surface O₃ at GZ_ZL and GZ_NS is likely linked to local emissions combined with weak dispersion (Yang et al., 2020; Zhou et al., 2022). North China stations (CAMS1, CAMS2, UCAS, WD, SJZ_LC and SXU) display a typical urban O₃ diurnal pattern. At CAMS1 and CAMS2, O₃ in the 0–1 km layer reaches 80–120 ppb in the morning (08:00–10:00) and decreases markedly in the early afternoon, reflecting rapid boundary-layer growth and



438 photochemical loss after sunrise (David and Nair, 2011; Liao et al., 2023). UCAS and
439 WD show similar morning maxima, whereas SJZ_LC is characterized by lower and
440 more stable O₃, indicative of relatively clean background conditions. At SXU, high
441 morning O₃ (80–100 ppb) is followed by even higher afternoon levels (>100 ppb),
442 pointing to strong in situ secondary production under intense photochemical activity
443 (Wang et al., 2017; Xia et al., 2021). East China sites (TS, NUIST, LA, HNU, AHU
444 and CF) exhibit more complex diurnal behaviour. At TS, O₃ peaks at 1–2 km during
445 12:00–15:00 (80–100 ppb), suggesting an important role of vertical transport and
446 local emissions. NUIST and AHU show morning maxima similar to those in North
447 China, whereas LA maintains low and weakly varying O₃, consistent with relatively
448 clean conditions (Chen et al., 2024). At HNU, near-surface O₃ increases in the early
449 afternoon (60–80 ppb), reflecting active photochemistry (Wang et al., 2025c). CF
450 shows a pronounced afternoon peak (13:00–17:00, 80–120 ppb), indicating a strong
451 influence of local sources (Xia et al., 2021; Yang et al., 2020). South China sites (GIG,
452 SUST, GZ_ZL, GZ_NS, GZ_TM, GZ_GY and GZ_DXC) differ substantially from
453 those in the north and east. GIG exhibits low and weakly varying O₃, representative of
454 background conditions (Chen et al., 2024; Lin et al., 2022). The other sites show
455 morning near-surface maxima (80–100 ppb at 08:00–10:00), followed by decreases
456 associated with rapid boundary-layer development after sunrise (David and Nair, 2011;
457 Liao et al., 2023), and enhanced O₃ at 3–4 km in the afternoon (13:00–17:00),
458 highlighting the pronounced vertical structure of O₃ pollution in this region.
459 Southwestern sites (CDAES and CQ) display distinct afternoon enhancements at 1–2
460 km. At CDAES, O₃ reaches 80–120 ppb during 15:00–18:00, likely favoured by high
461 temperature and humidity that accelerate photochemical production (Yang et al., 2020;
462 Zhang et al., 2022), while CQ shows a similar but weaker enhancement (60–80 ppb).
463 The central China site LY exhibits morning near-surface maxima (60–80 ppb) and
464 elevated O₃ at 2–4 km in the afternoon, characteristic of a typical urban diurnal cycle.
465 Seasonal mean diurnal vertical profiles are shown in Figures S13–S16. These regional
466 contrasts underline the differing controls on O₃ across China, with strong local
467 photochemistry in North China, combined regional transport and sustained
468 photochemical production in South China, and mixed influences of emissions and
469 meteorology in East China.



470

471

Figure 6. Mean diurnal vertical profiles of O₃ for 2021–2024.

472

473

3.3 OH production

474

Photolysis of HONO and O₃ constitutes a primary source of OH radicals and therefore controls the atmospheric oxidation capacity (AOC). To quantify the AOC at each site, we evaluated altitude-resolved OH production from HONO and O₃ using in situ concentration profiles combined with photolysis frequencies calculated by the TUV model. OH production from HONO and O₃ was computed from the following expressions.

480

$$P(OH)_{HONO} = J(HONO) \times [HONO] \quad (2)$$

481

$$P(OH)_{O_3} = 2 \times f \times J(O(^1D)) \times [O_3] \quad (3)$$

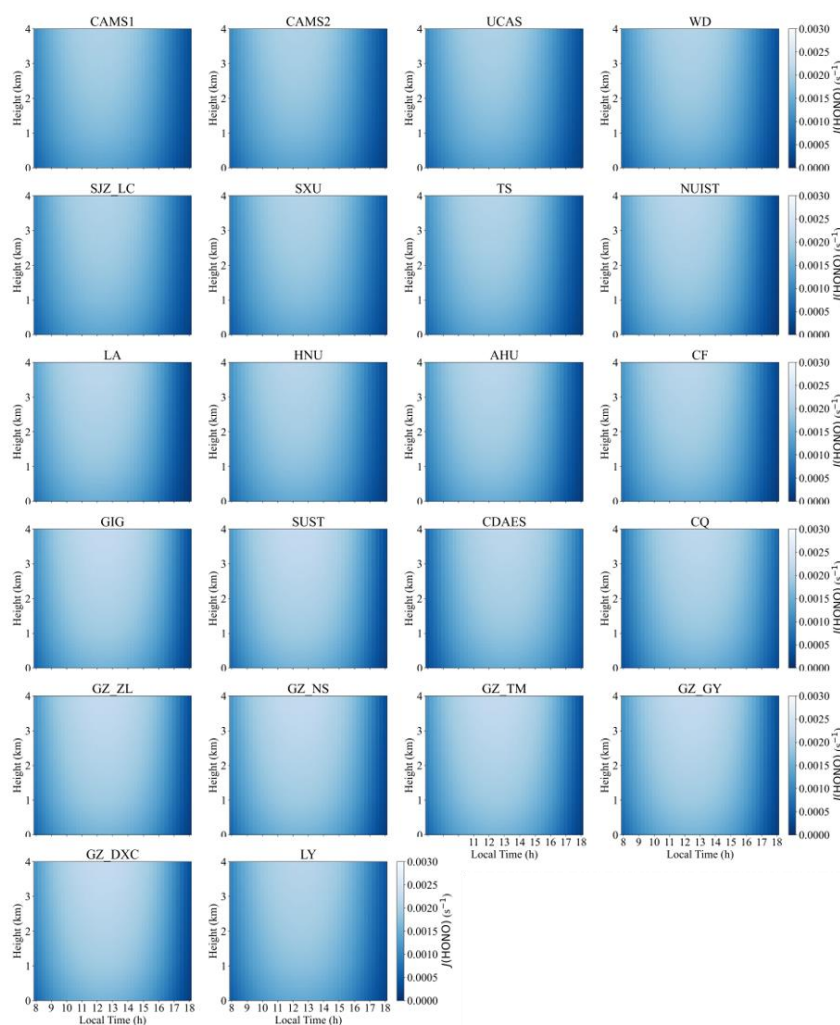


482 Here, $J(\text{HONO})$ and $J(\text{O}(^1\text{D}))$ are the photolysis rate coefficients of HONO and O_3 ,
483 respectively, obtained from the TUV model. $\text{O}(^1\text{D})$ denotes electronically excited
484 atomic oxygen produced by O_3 photodissociation, and f represents the branching
485 fraction of the reaction $\text{O}(^1\text{D}) + \text{H}_2\text{O} \rightarrow 2\text{OH}$. $[\text{HONO}]$ and $[\text{O}_3]$ are the
486 concentrations of HONO and O_3 at each altitude level.

487 Figure 7 presents the mean diurnal vertical profiles of the HONO photolysis
488 frequency, $J(\text{HONO})$, at 22 sites during 2021–2024; the corresponding seasonal mean
489 diurnal variations are presented in Figures S17–S20. All sites exhibit a canonical
490 photochemical pattern: $J(\text{HONO})$ increases rapidly after sunrise, reaches a maximum
491 around local noon, and then gradually decreases with increasing solar zenith angle.
492 Elevated values persist between 10:00 and 14:00 local time, with peak $J(\text{HONO})$
493 typically occurring near 12:00–13:00, indicating that HONO photolysis is primarily
494 controlled by solar irradiance, in agreement with observations in Beijing and
495 Guangzhou (He et al., 2023c; Ryan et al., 2018). Vertically, $J(\text{HONO})$ increases
496 systematically with altitude. Photolysis rates are relatively low in the near-surface
497 layer (0–0.5 km), increase markedly in the upper mixed layer and lower free
498 troposphere (approximately 1–3 km), and reach maxima between 2 and 4 km, with
499 peak values around $2.5 \times 10^{-3} \text{ s}^{-1}$. This “weaker near the surface and stronger aloft”
500 structure is highly consistent with the $J(\text{HONO})$ profiles reported by Xing et al.
501 (2024a) and reflects the combined effects of aerosol attenuation of ultraviolet
502 radiation in the lower atmosphere and enhanced shortwave actinic flux at higher
503 altitudes (He et al., 2023c; Ryan et al., 2018; Spataro and Ianniello, 2014). At the
504 North China sites (CAMS1, CAMS2, UCAS, WD, SJZ_LC, SXU), $J(\text{HONO})$ exhibits
505 a pronounced diurnal cycle, increasing during the morning (08:00–10:00) with rising
506 solar radiation, peaking at midday (12:00–14:00) at $0.0020\text{--}0.0025 \text{ s}^{-1}$, and decreasing
507 in the afternoon (14:00–18:00). The urban Beijing sites CAMS1 and CAMS2 show
508 peak values of $\sim 0.0025 \text{ s}^{-1}$, comparable to those at other North China Plain stations
509 (e.g., UCAS and WD), reflecting strong photolysis under high HONO loading and
510 favourable radiation conditions. At SJZ_LC, located at the foothills of the Taihang
511 Mountains, morning $J(\text{HONO})$ is slightly enhanced, likely owing to temperature
512 inversions that modulate the vertical distribution of aerosols and actinic flux. The
513 elevated site SXU (780 m a.s.l.) exhibits systematically higher $J(\text{HONO})$ than lowland
514 stations, with a peak of $\sim 0.0022 \text{ s}^{-1}$, consistent with reduced aerosol extinction and
515 stronger solar radiation at higher altitude. East China sites (TS, NUIST, LA, HNU,
516 AHU, CF) display similar peak timing to North China but slightly lower magnitudes
517 ($0.0015\text{--}0.0025 \text{ s}^{-1}$). For example, $J(\text{HONO})$ at NUIST peaks at $\sim 0.0020 \text{ s}^{-1}$, whereas
518 the high-altitude background site TS (1500 m a.s.l.) reaches $\sim 0.0021 \text{ s}^{-1}$, consistent
519 with enhanced actinic flux under cleaner atmospheric conditions. In South China
520 (GIG, SUST, GZ_ZL, GZ_NS, GZ_TM, GZ_GY, GZ_DXC), the maximum $J(\text{HONO})$
521 occurs slightly later in the day (13:00–15:00) and attains higher values (0.0020--
522 0.0030 s^{-1}). The highest peak is observed at GZ_DXC ($\sim 0.0030 \text{ s}^{-1}$), likely reflecting
523 elevated HONO concentrations promoted by warm and humid conditions that favour



524 heterogeneous formation. The southwestern basin site CQ shows a comparable peak
525 ($\sim 0.0025 \text{ s}^{-1}$), while the Central China site LY reaches $\sim 0.0020 \text{ s}^{-1}$, similar to values in
526 North and East China. Overall, urban sites exhibit larger diurnal amplitudes and 20–
527 40% higher $J(\text{HONO})$ maxima than mountain or clean-background sites, owing to
528 higher HONO abundances and aerosol loading that modulate the effective actinic flux.
529 This behaviour is fully consistent with previous findings from Beijing, Shanghai and
530 other megacities, which reported pronounced daytime enhancement of $J(\text{HONO})$
531 under high- NO_2 and high-HONO conditions (He et al., 2023c; Spataro and Ianniello,
532 2014; Ye et al., 2023).



533

534 Figure 7. Mean diurnal vertical profiles of the HONO photolysis rate, $J(\text{HONO})$.

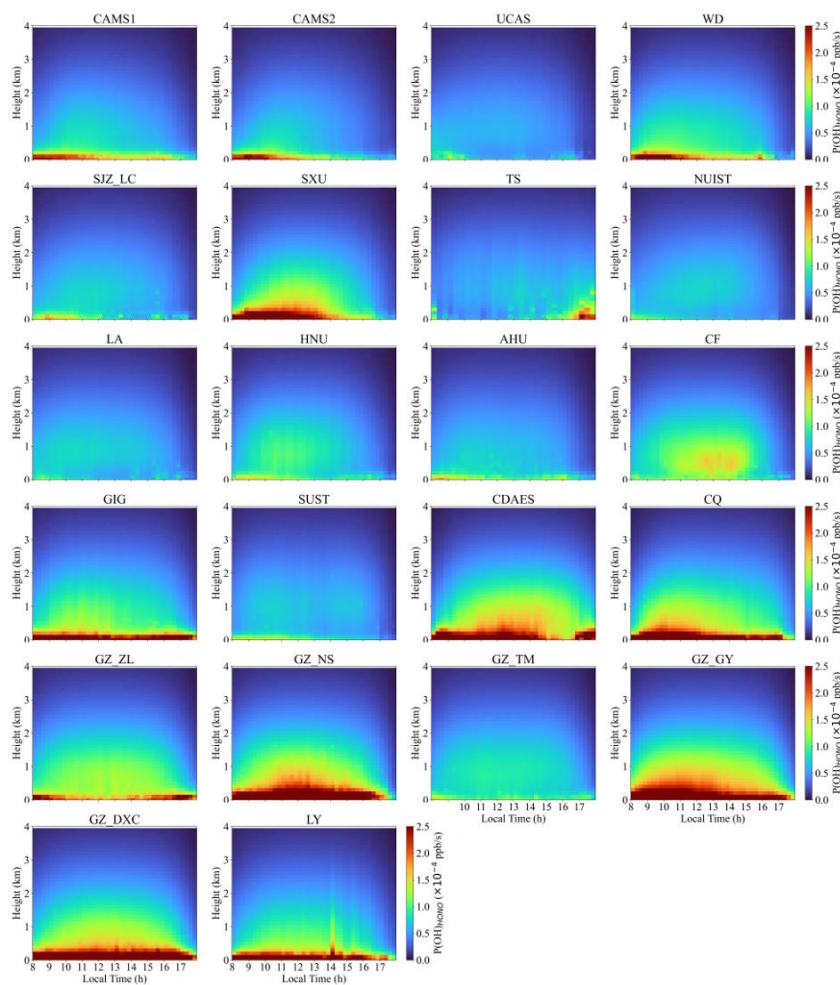
535 Figure 8 presents the mean diurnal vertical profiles of OH production from
536 HONO photolysis, $P(\text{OH})_{\text{HONO}}$, at 22 sites; the corresponding seasonal mean profiles



537 are shown in Figures S21–S24. At all sites, $P(\text{OH})_{\text{HONO}}$ displays a pronounced
538 unimodal diurnal cycle, increasing rapidly after sunrise, peaking between 10:00 and
539 14:00, and declining thereafter. The peak timing closely follows the maximum of the
540 $J(\text{HONO})$, whereas the peak altitude remains confined to the near-surface layer,
541 reflecting the strong surface enhancement of HONO. In the lower boundary layer (0–
542 0.5 km), $P(\text{OH})_{\text{HONO}}$ attains its column maximum, with most sites peaking between
543 11:00 and 13:00 and reaching 1.0×10^4 – 5.5×10^4 ppb s^{-1} . For all stations, $P(\text{OH})_{\text{HONO}}$ is
544 largest within 0–1 km and decreases monotonically with height, consistent with the
545 preferential accumulation of HONO near the surface and the resulting localization of
546 photochemically produced OH (He et al., 2023c; Li et al., 2025b; Xing et al., 2021b;
547 Zhang et al., 2025a). Several sites, including SXU, CDAES, CQ, GZ_NS, GZ_GY,
548 and GZ_DXC, exhibit particularly strong OH production, with peak $P(\text{OH})_{\text{HONO}}$
549 commonly exceeding 3.0×10^4 ppb s^{-1} . This reflects the combined effects of elevated
550 HONO levels and intense solar radiation. At these locations, the high- $P(\text{OH})_{\text{HONO}}$
551 layer can extend to 1–2 km, indicating a deeper photochemically active region. This
552 feature is consistent with earlier reports highlighting the substantial contribution of
553 HONO to OH in the lower free troposphere (Aumont et al., 2003; R. Crilley et al.,
554 2016; Xue et al., 2025; Zhang et al., 2025a). Vertically, $P(\text{OH})_{\text{HONO}}$ decreases rapidly
555 with altitude at all sites and is reduced to 20–40% of its surface value above 2 km,
556 demonstrating that the impact of HONO photolysis on OH is largely confined to the
557 boundary layer. In agreement with previous observations in Beijing and Guangzhou
558 (Gu et al., 2022; Meng et al., 2020; Yu et al., 2022), HONO photolysis represents one
559 of the dominant OH sources during the morning and around local noon, accounting
560 for 30–60% of the daytime OH production near the surface (Song et al., 2023a; Tang
561 et al., 2015). In the present study, several plateau sites show even larger relative
562 contributions at midday, indicating that under conditions of low NO_2 and strong solar
563 irradiance, HONO photolysis becomes an especially efficient radical source,
564 consistent with findings at Nam Co (Xing et al., 2024b). Regionally, North China sites
565 (CAMS1, CAMS2, UCAS, WD, SJZ_LC, and SXU) exhibit near-surface (0–1 km)
566 $P(\text{OH})_{\text{HONO}}$ maxima between 12:00 and 14:00 local time, with values of 1.0×10^4 –
567 3.0×10^4 ppb s^{-1} . At CAMS1, the peak reaches $\sim 1.5 \times 10^4$ ppb s^{-1} , whereas at SJZ_LC,
568 although nocturnal temperature inversions near the Taihang Mountains may favour
569 HONO accumulation, the peak remains modest ($\sim 1.2 \times 10^4$ ppb s^{-1}) owing to weaker
570 local emissions, comparable to UCAS and WD (1.0×10^4 – 2.5×10^4 ppb s^{-1}). At these
571 sites, $P(\text{OH})_{\text{HONO}}$ declines sharply with height and is substantially reduced above 1
572 km, underscoring the near-surface confinement of both HONO and its photolytic OH
573 production. East China stations (TS, NUIST, LA, HNU, AHU, and CF) show similar
574 peak times (12:00–14:00) but slightly lower magnitudes (1.0×10^4 – 1.5×10^4 ppb s^{-1}).
575 In South China (GIG, SUST, GZ_ZL, GZ_NS, GZ_TM, GZ_GY, and GZ_DXC),
576 peaks occur later (13:00–15:00) and are substantially higher (2.5×10^4 – 5.5×10^4 ppb
577 s^{-1}), consistent with enhanced heterogeneous HONO formation under warm and
578 humid conditions. Southwest China sites (CDAES and CQ) reach peak values of



579 $\sim 3.5 \times 10^{-4}$ ppb s^{-1} , comparable to those in South China, likely owing to basin-induced
580 HONO accumulation and vigorous photochemistry. In Central China (LY), the peak
581 ($\sim 2.7 \times 10^{-4}$ ppb s^{-1}) is similar to that in North and East China, indicating broadly
582 comparable HONO sources and photolysis efficiencies across these regions.



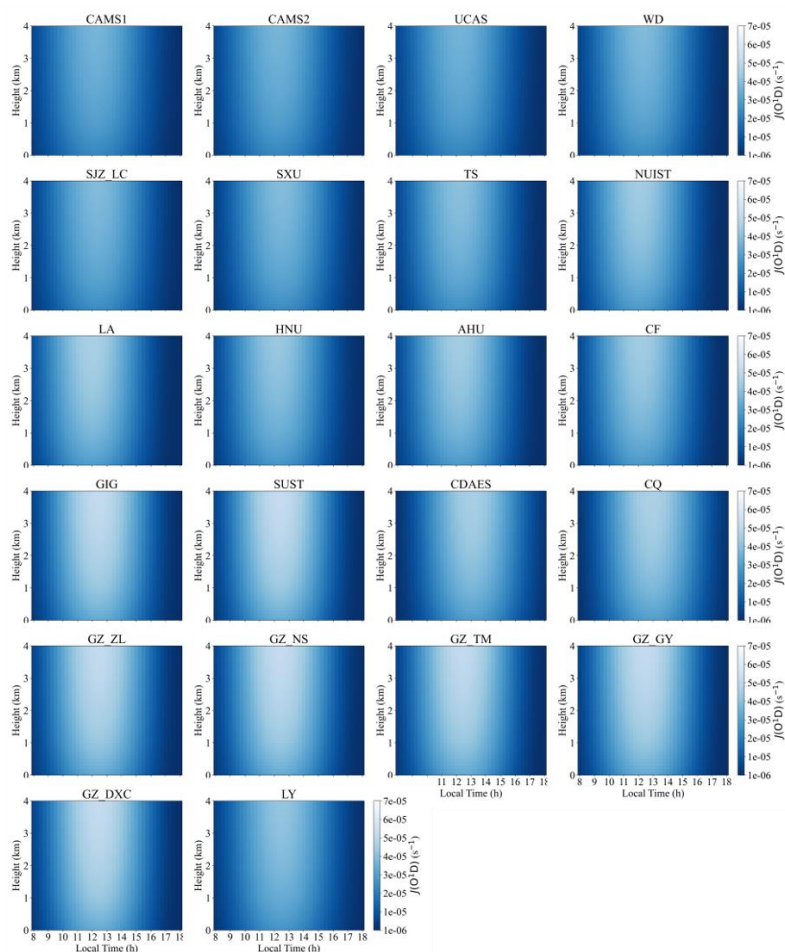
583

584 Figure 8. Mean vertical profiles of OH radicals generated by HONO photolysis.

585 Figure 9 presents the O_3 photolysis frequency, $J(O(^1D))$, at all 22 sites follows a
586 pronounced diurnal cycle, with maxima consistently occurring between 12:00 and
587 14:00 local time. Seasonal mean diurnal variations are presented in Figures S25–S28.
588 In North China (CAMS1, CAMS2, UCAS, WD, SJZ_LC, and SXU), near-surface
589 peak $J(O(^1D))$ ranges from $\sim 5 \times 10^{-5}$ to 7×10^{-5} s^{-1} . The urban sites CAMS1, CAMS2,
590 UCAS, and WD reach the highest values ($\sim 6 \times 10^{-5}$ – 7×10^{-5} s^{-1}) at midday. At SJZ_LC,
591 located at the foothills of the Taihang Mountains, nocturnal temperature inversions
592 can favour O_3 accumulation (Guo et al., 2024b; He et al., 2021), but the peak remains



593 slightly lower ($\sim 5 \times 10^{-5}$ – 6×10^{-5} s⁻¹), likely constrained by local emissions. At the
594 higher-altitude SXU site (780 m a.s.l.), near-surface $J(\text{O}(^1\text{D}))$ is reduced ($\sim 4 \times 10^{-5}$ –
595 5×10^{-5} s⁻¹). Overall, urban stations exhibit larger $J(\text{O}(^1\text{D}))$ than suburban and rural
596 sites, reflecting higher O₃ levels driven by anthropogenic precursors and consistent
597 with reported regional contrasts (Fardilah et al., 2023; Guo et al., 2024a; Qiu et al.,
598 2025). In East China (TS, NUIST, LA, HNU, AHU, and CF), near-surface $J(\text{O}(^1\text{D}))$
599 peaks at $\sim 4 \times 10^{-5}$ – 6×10^{-5} s⁻¹, with urban sites such as NUIST and AHU reaching
600 $\sim 5 \times 10^{-5}$ – 6×10^{-5} s⁻¹ at noon. In contrast, the high-altitude TS site (1500 m a.s.l.)
601 shows lower values ($\sim 3 \times 10^{-5}$ – 4×10^{-5} s⁻¹), consistent with its lower O₃ burden and
602 cleaner background conditions. South China stations (GIG, SUST, GZ_ZL, GZ_NS,
603 GZ_TM, GZ_GY, and GZ_DXC) display slightly higher peak $J(\text{O}(^1\text{D}))$ ($\sim 6 \times 10^{-5}$ –
604 7×10^{-5} s⁻¹), in line with enhanced O₃ production under warm and humid subtropical
605 conditions (Lu et al., 2025; Song et al., 2026; Zhang et al., 2025b). In Southwest
606 China (CDAES and CQ), peak values ($\sim 5 \times 10^{-5}$ – 6×10^{-5} s⁻¹) are comparable to those in
607 South China, likely driven by basin topography that favours O₃ accumulation and
608 vigorous photochemistry (Qiao et al., 2019; Shu et al., 2023; Wang et al., 2024a). The
609 Central China site LY exhibits slightly lower peaks ($\sim 4 \times 10^{-5}$ – 5×10^{-5} s⁻¹), similar to
610 North and East China, indicating broadly comparable O₃ sources and photolysis
611 efficiencies across these regions.



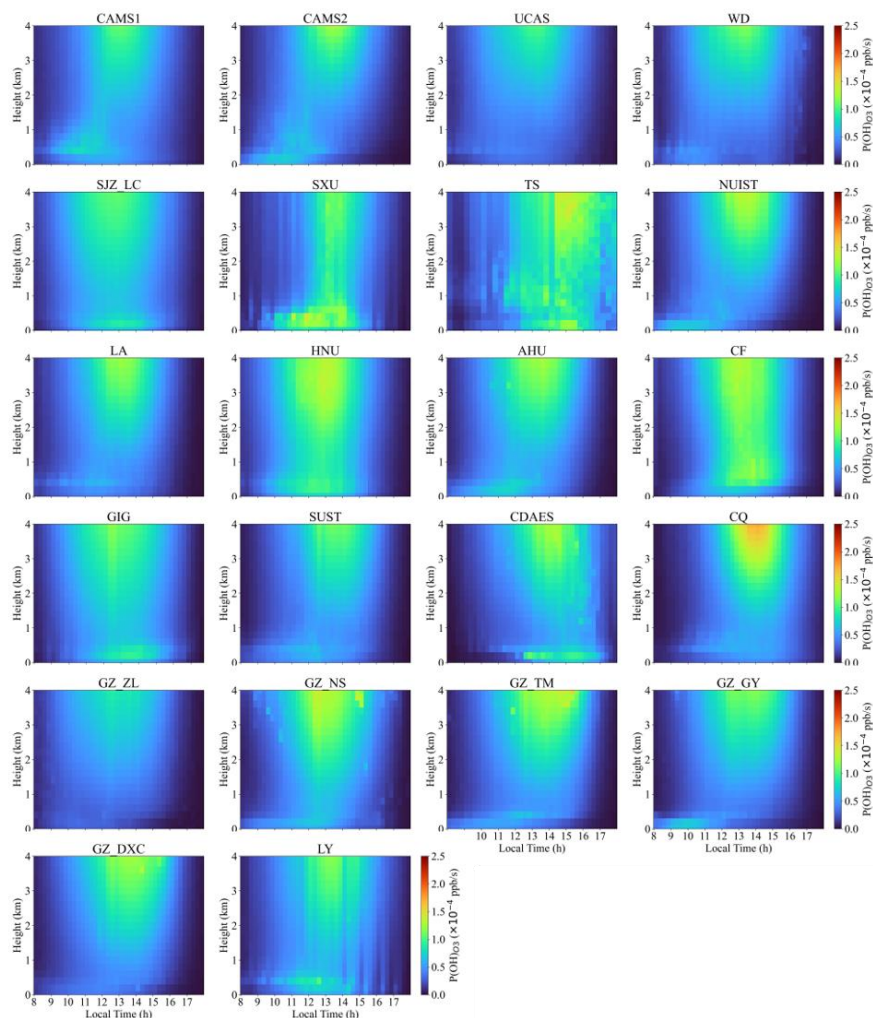
612

613 Figure 9. Mean diurnal vertical profiles of the O_3 photolysis rate, $J(O(^1D))$.

614 Figure 10 presents the mean diurnal vertical profiles of the OH production rate
615 from ozone photolysis, $P(OH)_{O_3}$, at the 22 sites, and seasonal mean diurnal
616 variations are presented in Figures S29–S32. All sites exhibit a pronounced unimodal
617 diurnal cycle, with $P(OH)_{O_3}$ increasing rapidly after sunrise, peaking between 12:00
618 and 14:00 local time, and declining thereafter. The vertical location of the maxima
619 varies markedly among sites: at some, enhanced production is confined to the near-
620 surface layer (0–0.5 km), whereas at others distinct maxima occur at 3–4 km,
621 indicating substantial regional differences in photochemical regimes. Peak $P(OH)_{O_3}$
622 spans 0.5×10^{-4} – 2.0×10^{-4} ppb s^{-1} across the network. In North China (CAMS1,
623 CAMS2, UCAS, WD, SJZ_LC, and SXU), near-surface $P(OH)_{O_3}$ during 12:00–14:00
624 reaches 1.0×10^{-4} – 2.0×10^{-4} ppb s^{-1} . The urban sites CAMS1, CAMS2, UCAS, and
625 WD show the highest values (1.5×10^{-4} – 2.0×10^{-4} ppb s^{-1}), whereas SJZ_LC, likely
626 influenced by local emissions and complex topography, exhibits slightly lower peaks



627 (1.0×10^{-4} – 1.5×10^{-4} ppb s⁻¹). SXU reaches $\sim 1.7 \times 10^{-4}$ ppb s⁻¹. At all these sites,
628 P(OH)₃ decreases with altitude and generally falls below 1.0×10^{-4} ppb s⁻¹ above 1
629 km. East China stations (TS, NUIST, LA, HNU, AHU, and CF) display similar peak
630 timing (12:00–14:00), with near-surface maxima of 1.0×10^{-4} – 1.8×10^{-4} ppb s⁻¹. TS,
631 NUIST, HNU, AHU, and CF reach $\sim 1.5 \times 10^{-4}$ – 1.8×10^{-4} ppb s⁻¹, while LA peaks at
632 $\sim 1.4 \times 10^{-4}$ ppb s⁻¹. In South China (GIG, SUST, GZ_ZL, GZ_NS, GZ_TM, GZ_GY,
633 and GZ_DXC), the maxima occur slightly later (13:00–15:00) and are generally
634 higher (1.3×10^{-4} – 1.7×10^{-4} ppb s⁻¹), with GZ_GY reaching $\sim 1.9 \times 10^{-4}$ ppb s⁻¹ and
635 GZ_NS, GZ_TM, and GZ_DXC $\sim 1.8 \times 10^{-4}$ ppb s⁻¹. Southwest China (CDAES and
636 CQ) shows peaks of $\sim 1.5 \times 10^{-4}$ – 2.5×10^{-4} ppb s⁻¹, including $\sim 1.9 \times 10^{-4}$ ppb s⁻¹ at CQ
637 and $\sim 1.5 \times 10^{-4}$ ppb s⁻¹ at CDAES. The Central China site LY exhibits a peak of
638 $\sim 1.5 \times 10^{-4}$ ppb s⁻¹, comparable to those in North and East China, indicating broadly
639 similar ozone photochemical efficiencies across these regions.



640

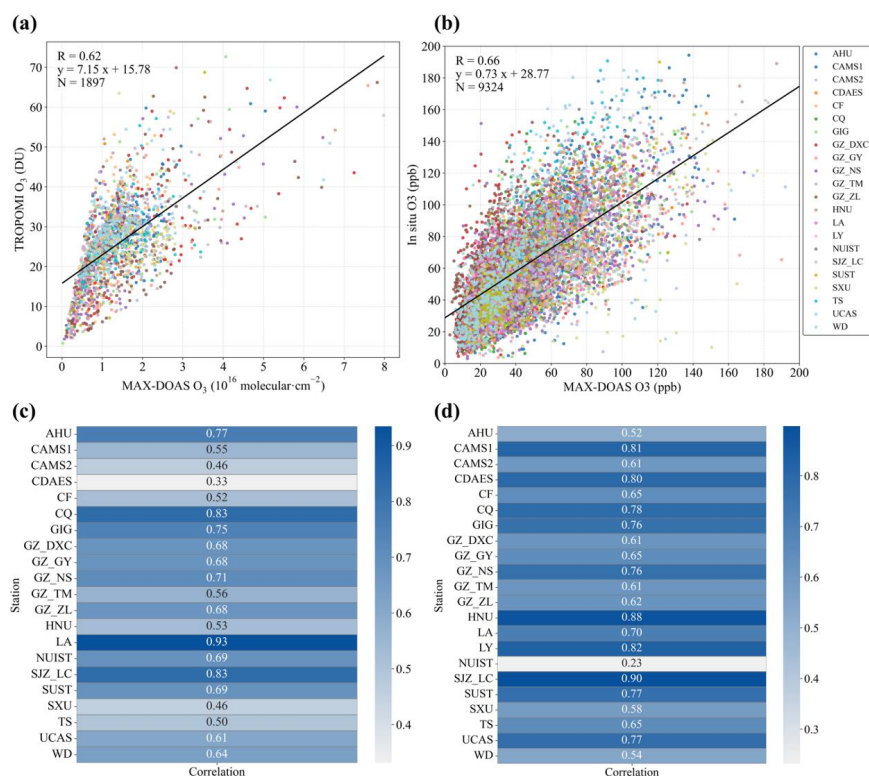


641 Figure 10. Mean vertical profiles of OH radicals produced by O₃ photolysis.

642

643 **3.4 Validations with independent data**

644 The dataset was validated using two independent approaches. First, O₃ VCD
645 retrieved from the MAX-DOAS network for 2021–2024 were evaluated against
646 coincident TROPOMI satellite observations. MAX-DOAS measurements were
647 averaged within ±30 min of the TROPOMI overpass (13:30–14:00 Beijing Time), and
648 TROPOMI pixels were spatially averaged over a 7 km × 5.5 km area center on each
649 site, consistent with the native spatial resolution of TROPOMI. As shown in Figure
650 11a, the two datasets exhibit a strong linear relationship, with a Pearson correlation
651 coefficient of $R = 0.62$ ($N = 1897$); site-resolved correlations are given in Figure 11c.
652 Second, near-surface O₃ concentrations retrieved at the 22 hyperspectral sites were
653 compared with in situ measurements from the nearest CNEMC over the same period.
654 Site pairs were selected following the spatial representativeness criteria of Song et al.
655 (2023b), and the separation distances are listed in Table S1; pairs that did not satisfy
656 the matching requirements were excluded. The comparison (Figure 11b) shows a
657 significant positive correlation ($R = 0.66$, $N = 9324$), demonstrating good consistency
658 between MAX-DOAS-derived surface O₃ and ground-based observations. The
659 correlations for each hyperspectral site and its nearest CNEMC are summarized in
660 Figure 11d. Together, these two independent validations confirm the reliability of the
661 dataset used in this study.



662
 663 Figure 11. (a) Correlation between O₃ column densities retrieved from hyperspectral
 664 ground-based stations and TROPOMI satellite observations; (b) correlation between
 665 hyperspectral O₃ column densities and in situ O₃ measurements from the nearest
 666 CNEMC; (c) site-specific correlations between hyperspectral and TROPOMI O₃
 667 column densities; (d) site-specific correlations between hyperspectral O₃ column
 668 densities and in situ O₃ at the nearest CNEMC.

669

670 **4. Data availability**

671 The vertical profiles of HONO and O₃, and the vertical profiles of OH radicals
 672 over the major regions of China presented in this study, are freely available in .xlsx
 673 format at Zenodo (<https://doi.org/10.5281/zenodo.18489836>; Zou et al., 2026).

674

675 **5. Summary**

676 We developed and released a comprehensive dataset of vertical profiles of
 677 HONO and O₃, and the associated OH radical production rates, P(OH)_{HONO} and
 678 P(OH)_{O₃}, derived from the Chinese hyperspectral vertical remote-sensing network for
 679 2021–2024. The dataset spans 22 representative sites across North, East, Central,
 680 South, and Southwest China, covering a wide range of climatic regimes and surface
 681 types, and represents one of the most extensive collections in China in terms of spatial



682 coverage and vertical resolution of photochemical parameters relevant to OH
683 precursors. Independent validation against TROPOMI satellite retrievals and in situ
684 measurements from the CNEMC demonstrates robust consistency. Mean diurnal
685 profiles within 0–4 km reveal pronounced regional and vertical contrasts in HONO
686 and O₃ driven photochemistry. Both J(HONO) and J(O(¹D)) exhibit radiation
687 controlled, single-peaked diurnal cycles, with maxima around local noon (11:00–
688 14:00), and remain elevated in the upper mixed layer and the lower free troposphere,
689 reflecting the combined effects of radiative transfer and aerosol extinction on the
690 vertical distribution of photolysis rates. Accordingly, P(OH)_{HONO} and P(OH)_{O₃} peak
691 near the surface and decrease with height, indicating that the boundary layer is the
692 primary daytime source region of OH. At several plateau and mountainous sites,
693 however, the lower free troposphere also shows a substantial radical production
694 potential. Urban and highly industrialized sites exhibit higher photolysis rates and OH
695 production, reflecting the combined effects of high precursor concentrations and
696 strong radiation, while high-altitude clean-background sites, despite lower near-
697 surface concentrations, maintain relatively large photolysis rates and significant OH
698 production at middle and upper levels due to weaker aerosol extinction and stronger
699 shortwave radiation, showing a vertical photochemical structure distinct from that
700 over plains.

701 With continuous temporal coverage ranging from five months to 3.5 years and
702 multi-site vertical profiling, this dataset provides a valuable foundation for: (1)
703 quantifying the relative contributions of HONO and O₃ photolysis to the OH budget
704 in the boundary layer and the lower free troposphere; (2) constraining radical initial
705 conditions and radiative parameterizations in regional and global chemical transport
706 models; (3) enabling cross-validation and synergistic inversion among ground-based,
707 UAV, and satellite observations; (4) advancing studies of photochemical pollution
708 formation, secondary aerosol production, and atmospheric oxidation capacity; and (5)
709 supporting air-quality management and policy development as a complementary
710 national monitoring resource.

711

712 **Financial support**

713 This work was supported by the National Natural Science Foundation of China
714 (42588301, 42225504), the President's Foundation of Hefei Institutes of Physical
715 Science, Chinese Academy of Sciences (YZJJQY202401, BJPY2024B09).

716

717 **Author contributions**

718 All the authors were involved in the generation of the introduced dataset. TZ, CX and
719 CL wrote the manuscript with contributions from all the other authors.

720

721 **References**

722 Aliwell, S. R., Van Roozendaal, M., Johnston, P. V., Richter, A., Wagner, T., Arlander, D. W.,
723 Burrows, J. P., Fish, D. J., Jones, R. L., Tørnkvist, K. K., Lambert, J.-C., Pfeilsticker, K., and



- 724 Pundt, I.: Analysis for BrO in zenith-sky spectra: An intercomparison exercise for analysis
725 improvement, *Journal of Geophysical Research: Atmospheres*, 107, ACH 10-1-ACH 10-20,
726 <https://doi.org/10.1029/2001JD000329>, 2002.
- 727 Ancellet, G., Viatte, C., Boynard, A., Ravetta, F., Pelon, J., Cailteau-Fischbach, C., Genau, P.,
728 Capo, J., Roy, A., and Nédélec, P.: Analysis of the day-to-day variability of ozone vertical
729 profiles in the lower troposphere during the 2022 Paris ACROSS campaign, *Atmospheric
730 Chemistry and Physics*, 24, 12963–12983, <https://doi.org/10.5194/acp-24-12963-2024>, 2024.
- 731 Andersen, S. T., Carpenter, L. J., Reed, C., Lee, J. D., Chance, R., Sherwen, T., Vaughan, A. R.,
732 Stewart, J., Edwards, P. M., Bloss, W. J., Sommariva, R., Crilley, L. R., Nott, G. J., Neves, L.,
733 Read, K., Heard, D. E., Seakins, P. W., Whalley, L. K., Boustead, G. A., Fleming, L. T.,
734 Stone, D., and Fomba, K. W.: Extensive field evidence for the release of HONO from the
735 photolysis of nitrate aerosols, *Science Advances*, 9, eadd6266,
736 <https://doi.org/10.1126/sciadv.add6266>, 2023.
- 737 Anon: Systematic Evaluation of Four Satellite AOD Datasets for Estimating PM2.5 Using a
738 Random Forest Approach, *Remote sensing*, 15, 2064–2064,
739 <https://doi.org/10.3390/rs15082064>, 2023.
- 740 Aumont, B., Chervier, F., and Laval, S.: Contribution of HONO sources to the NO_x/HO_x/O₃
741 chemistry in the polluted boundary layer, *Atmospheric Environment*, 37, 487–498,
742 [https://doi.org/10.1016/S1352-2310\(02\)00920-2](https://doi.org/10.1016/S1352-2310(02)00920-2), 2003.
- 743 Chambers, S. D., Guérette, E.-A., Monk, K., Griffiths, A. D., Zhang, Y., Duc, H., Cope, M.,
744 Emmerson, K. M., Chang, L. T., Silver, J. D., Utembe, S., Crawford, J., Williams, A. G., and
745 Keyword, M.: Skill-Testing Chemical Transport Models across Contrasting Atmospheric
746 Mixing States Using Radon-222, *Atmosphere*, 10, 25,
747 <https://doi.org/10.3390/atmos10010025>, 2019.
- 748 Chen, Z., Xie, Y., Liu, J., Shen, L., Cheng, X., Han, H., Yang, M., Shen, Y., Zhao, T., and Hu, J.:
749 Distinct seasonality in vertical variations of tropospheric ozone over coastal regions of
750 southern China, *Science of The Total Environment*, 874, 162423,
751 <https://doi.org/10.1016/j.scitotenv.2023.162423>, 2023.
- 752 Chen, Z., Liu, R., Wu, S., Xu, J., Wu, Y., and Qi, S.: Diurnal variation characteristics and
753 meteorological causes of autumn ozone in the Pearl River Delta, China, *Science of The Total
754 Environment*, 908, 168469, <https://doi.org/10.1016/j.scitotenv.2023.168469>, 2024.
- 755 Couillard, M. H., Schwab, M. J., Schwab, J. J., Lu, C.-H. (Sarah), Joseph, E., Stutsrim, B.,
756 Shrestha, B., Zhang, J., Knepp, T. N., and Gronoff, G. P.: Vertical Profiles of Ozone
757 Concentrations in the Lower Troposphere Downwind of New York City During LISTOS
758 2018–2019, *Journal of Geophysical Research: Atmospheres*, 126, e2021JD035108,
759 <https://doi.org/10.1029/2021JD035108>, 2021.
- 760 David, L. M. and Nair, P. R.: Diurnal and seasonal variability of surface ozone and NO_x at a
761 tropical coastal site: Association with mesoscale and synoptic meteorological conditions,
762 *Journal of Geophysical Research: Atmospheres*, 116, <https://doi.org/10.1029/2010JD015076>,
763 2011.
- 764 Dewan, S. and Lakhani, A.: Tropospheric ozone and its natural precursors impacted by climatic
765 changes in emission and dynamics, *Front. Environ. Sci.*, 10,



- 766 <https://doi.org/10.3389/fenvs.2022.1007942>, 2022.
- 767 Donzelli, G. and Suarez-Varela, M. M.: Tropospheric Ozone: A Critical Review of the Literature
768 on Emissions, Exposure, and Health Effects, *Atmosphere*, 15, 779,
769 <https://doi.org/10.3390/atmos15070779>, 2024.
- 770 Elshorbany, Y., Barnes, I., Becker, K., Kleffmann, J., and Wiesen, P.: Sources and cycling of
771 tropospheric hydroxyl radicals - An overview, USF St. Petersburg Campus Faculty
772 Publications, 2010.
- 773 Fardilah, R. D., Turyanti, A., Pangestu, L. A., Dominica, M. V., and Perdinan: Systematic
774 Literature Review on Ozone Dispersion Correlated with Diurnal Concentration Pattern in
775 Urban and Rural Areas, *Agromet*, 37, 77–90, <https://doi.org/10.29244/j.agromet.37.2.77-90>,
776 2023.
- 777 Fleischmann, O. C., Hartmann, M., Burrows, J. P., and Orphal, J.: New ultraviolet absorption
778 cross-sections of BrO at atmospheric temperatures measured by time-windowing Fourier
779 transform spectroscopy, *Journal of Photochemistry and Photobiology A: Chemistry*, 168,
780 117–132, <https://doi.org/10.1016/j.jphotochem.2004.03.026>, 2004.
- 781 Garcia-Nieto, D., Benavent, N., and Saiz-Lopez, A.: Measurements of atmospheric HONO
782 vertical distribution and temporal evolution in Madrid (Spain) using the MAX-DOAS
783 technique, *Science of The Total Environment*, 643, 957–966,
784 <https://doi.org/10.1016/j.scitotenv.2018.06.180>, 2018b.
- 785 Gu, R., Shen, H., Xue, L., Wang, T., Gao, J., Li, H., Liang, Y., Xia, M., Yu, C., Liu, Y., and Wang,
786 W.: Investigating the sources of atmospheric nitrous acid (HONO) in the megacity of Beijing,
787 China, *Science of The Total Environment*, 812, 152270,
788 <https://doi.org/10.1016/j.scitotenv.2021.152270>, 2022.
- 789 Guo, J., Zhang, X., Gao, Y., Wang, Z., Zhang, M., Xue, W., Herrmann, H., Brasseur, G. P., Wang,
790 T., and Wang, Z.: Evolution of Ozone Pollution in China: What Track Will It Follow?,
791 *Environ. Sci. Technol.*, 57, 109–117, <https://doi.org/10.1021/acs.est.2c08205>, 2023.
- 792 Guo, P., Su, Y., Sun, X., Liu, C., Cui, B., Xu, X., Ouyang, Z., and Wang, X.: Urban–Rural
793 Comparisons of Biogenic Volatile Organic Compounds and Ground-Level Ozone in Beijing,
794 *Forests*, 15, 508, <https://doi.org/10.3390/f15030508>, 2024a.
- 795 Guo, W., Yang, Y., Zhang, J., Han, K., Yang, Y., Chen, Q., Li, S., and Zhu, Y.: Effects of valley
796 topography on ozone pollution in the Lanzhou valley: A numerical case study, *Environ Pollut*,
797 363, 125225, <https://doi.org/10.1016/j.envpol.2024.125225>, 2024b.
- 798 Hao, Q., Jiang, N., Zhang, R., Yang, L., and Li, S.: Characteristics, sources, and reactions of
799 nitrous acid during winter at an urban site in the Central Plains Economic Region in China,
800 *Atmospheric Chemistry and Physics*, 20, 7087–7102, [https://doi.org/10.5194/acp-20-7087-](https://doi.org/10.5194/acp-20-7087-2020)
801 2020, 2020.
- 802 He, C., Wu, Q., Li, B., Liu, J., Gong, X., and Zhang, L.: Surface ozone pollution in China: Trends,
803 exposure risks, and drivers, *Front. Public Health*, 11,
804 <https://doi.org/10.3389/fpubh.2023.1131753>, 2023a.
- 805 He, G., He, C., Wang, H., Lu, X., Pei, C., Qiu, X., Liu, C., Wang, Y., Liu, N., Zhang, J., Lei, L.,
806 Liu, Y., Wang, H., Deng, T., Fan, Q., and Fan, S.: Nighttime ozone in the lower boundary
807 layer: insights from 3-year tower-based measurements in South China and regional air quality



- 808 modeling, *Atmospheric Chemistry and Physics*, 23, 13107–13124,
809 <https://doi.org/10.5194/acp-23-13107-2023>, 2023b.
- 810 He, S., Wang, S., Zhang, S., Zhu, J., Sun, Z., Xue, R., and Zhou, B.: Vertical distributions of
811 atmospheric HONO and the corresponding OH radical production by photolysis at the suburb
812 area of Shanghai, China, *Science of The Total Environment*, 858, 159703,
813 <https://doi.org/10.1016/j.scitotenv.2022.159703>, 2023c.
- 814 He, Y., Wang, H., Wang, H., Xu, X., Li, Y., and Fan, S.: Meteorology and topographic influences
815 on nocturnal ozone increase during the summertime over Shaoguan, China, *Atmospheric
816 Environment*, 256, 118459, <https://doi.org/10.1016/j.atmosenv.2021.118459>, 2021.
- 817 Hu, Q., Ji, X., Hong, Q., Li, J., Li, Q., Ou, J., Liu, H., Xing, C., Tan, W., Chen, J., Chang, B., and
818 Liu, C.: Vertical Evolution of Ozone Formation Sensitivity Based on Synchronous Vertical
819 Observations of Ozone and Proxies for Its Precursors: Implications for Ozone Pollution
820 Prevention Strategies, *Environ Sci Technol*, 58, 4291–4301,
821 <https://doi.org/10.1021/acs.est.4c00637>, 2024.
- 822 Itahashi, S., Mathur, R., Hogrefe, C., and Zhang, Y.: Modeling stratospheric intrusion and trans-
823 Pacific transport on tropospheric ozone using hemispheric CMAQ during April 2010 – Part 1:
824 Model evaluation and air mass characterization for stratosphere–troposphere transport,
825 *Atmospheric Chemistry and Physics*, 20, 3373–3396, [https://doi.org/10.5194/acp-20-3373-
826 2020](https://doi.org/10.5194/acp-20-3373-2020), 2020.
- 827 Ji, X., Liu, C., Wang, Y., Hu, Q., Lin, H., Zhao, F., Xing, C., Tang, G., Zhang, J., and Wagner, T.:
828 Ozone profiles without blind area retrieved from MAX-DOAS measurements and
829 comprehensive validation with multi-platform observations, *Remote Sensing of Environment*,
830 284, 113339, <https://doi.org/10.1016/j.rse.2022.113339>, 2023.
- 831 Johnson, M. S., Rozanov, A., Weber, M., Mettig, N., Sullivan, J., Newchurch, M. J., Kuang, S.,
832 Leblanc, T., Chouza, F., Berkoff, T. A., Gronoff, G., Strawbridge, K. B., Alvarez, R. J.,
833 Langford, A. O., Senff, C. J., Kirgis, G., McCarty, B., and Twigg, L.: TOLNet validation of
834 satellite ozone profiles in the troposphere: impact of retrieval wavelengths, *Atmospheric
835 Measurement Techniques*, 17, 2559–2582, <https://doi.org/10.5194/amt-17-2559-2024>, 2024.
- 836 Kim, H., Park, R. J., Hong, S.-Y., Park, D.-H., Kim, S.-W., Oak, Y. J., Feng, X., Lin, H., and Fu,
837 T.-M.: A mixed layer height parameterization in a 3-D chemical transport model:
838 Implications for gas and aerosol simulations, *Sci Total Environ*, 955, 176838,
839 <https://doi.org/10.1016/j.scitotenv.2024.176838>, 2024.
- 840 Li, K., Jacob, D. J., Shen, L., Lu, X., De Smedt, I., and Liao, H.: Increases in surface ozone
841 pollution in China from 2013 to 2019: anthropogenic and meteorological influences,
842 *Atmospheric Chemistry and Physics*, 20, 11423–11433, [https://doi.org/10.5194/acp-20-
843 11423-2020](https://doi.org/10.5194/acp-20-11423-2020), 2020.
- 844 Li, K., Tan, R., Qiao, W., Lee, T., Wang, Y., Zhang, D., Tang, M., Zhao, W., Gu, Y., Fan, S.,
845 Zhang, J., Lyu, X., Xue, L., Xu, J., Ma, Z., Latif, M. T., Amnuaylojaroen, T., Gil, J., Lee, M.-
846 H., Bak, J., Kim, J., Liao, H., Kanaya, Y., Lu, X., Nagashima, T., and Koo, J.-H.: Surface and
847 tropospheric ozone over East Asia and Southeast Asia from observations: distributions,
848 trends, and variability, *Atmospheric Chemistry and Physics*, 25, 11575–11596,
849 <https://doi.org/10.5194/acp-25-11575-2025>, 2025a.



- 850 Li, M., McDonald, B. C., McKeen, S. A., Eskes, H., Levelt, P., Francoeur, C., Harkins, C., He, J.,
851 Barth, M., Henze, D. K., Bela, M. M., Trainer, M., de Gouw, J. A., and Frost, G. J.:
852 Assessment of Updated Fuel-Based Emissions Inventories Over the Contiguous United States
853 Using TROPOMI NO₂ Retrievals, *Journal of Geophysical Research: Atmospheres*, 126,
854 e2021JD035484, <https://doi.org/10.1029/2021JD035484>, 2021.
- 855 Li, Y., Xing, C., Peng, H., Jiao, P., Zhang, Q., Liu, C., Sun, Z., Tan, W., and Liu, C.: Vertical
856 Differences in NO₂-to-HONO Heterogeneous Conversion and HONO-Driven OH
857 Production over Inland, Coastal, and Island Regions, *Environ. Sci. Technol.*, 59, 26020–
858 26030, <https://doi.org/10.1021/acs.est.5c10318>, 2025b.
- 859 Liao, Z., Pan, Y., Ma, P., Jia, X., Cheng, Z., Wang, Q., Dou, Y., Zhao, X., Zhang, J., and Quan, J.:
860 Meteorological and chemical controls on surface ozone diurnal variability in Beijing: A
861 clustering-based perspective, *Atmospheric Environment*, 295, 119566,
862 <https://doi.org/10.1016/j.atmosenv.2022.119566>, 2023.
- 863 Liao, Z., Gao, M., Zhang, J., Sun, J., Quan, J., Jia, X., Pan, Y., and Fan, S.: Mixing-layer-height-
864 referenced ozone vertical distribution in the lower troposphere of Chinese megacities:
865 stratification, classification, and meteorological and photochemical mechanisms,
866 *Atmospheric Chemistry and Physics*, 24, 3541–3557, [https://doi.org/10.5194/acp-24-3541-](https://doi.org/10.5194/acp-24-3541-2024)
867 2024, 2024.
- 868 Liao, Z., Zhang, J., Gao, M., and Ma, Z.: Widespread stratospheric intrusion influence on summer
869 ozone pollution over China revealed by multi-site ozonesonde and validated EAC4 reanalysis,
870 *Atmospheric Chemistry and Physics*, 25, 14865–14877, [https://doi.org/10.5194/acp-25-](https://doi.org/10.5194/acp-25-14865-2025)
871 14865-2025, 2025.
- 872 Lin, H., Xing, C., Hong, Q., Liu, C., Ji, X., Liu, T., Lin, J., Lu, C., Tan, W., Li, Q., and Liu, H.:
873 Diagnosis of Ozone Formation Sensitivities in Different Height Layers via MAX-DOAS
874 Observations in Guangzhou, *Journal of Geophysical Research: Atmospheres*, 127,
875 e2022JD036803, <https://doi.org/10.1029/2022JD036803>, 2022.
- 876 Liu, C., Xing, C., Hu, Q., Li, Q., Liu, H., Hong, Q., Tan, W., Ji, X., Lin, H., Lu, C., Lin, J., Liu, H.,
877 Wei, S., Chen, J., Yang, K., Wang, S., Liu, T., and Chen, Y.: Ground-Based Hyperspectral
878 Stereoscopic Remote Sensing Network: A Promising Strategy to Learn Coordinated Control
879 of O₃ and PM_{2.5} over China, *Engineering*, 19, 71–83,
880 <https://doi.org/10.1016/j.eng.2021.02.019>, 2022a.
- 881 Liu, H., Han, X., Tang, G., Zhang, J., Xia, X., Zhang, M., and Meng, L.: Model analysis of
882 vertical exchange of boundary layer ozone and its impact on surface air quality over the
883 North China Plain, *Science of The Total Environment*, 821, 153436,
884 <https://doi.org/10.1016/j.scitotenv.2022.153436>, 2022b.
- 885 Liu, P., Xue, C., Ye, C., Liu, C., Zhang, C., Wang, J., Zhang, Y., Liu, J., and Mu, Y.: The Lack of
886 HONO Measurement May Affect the Accurate Diagnosis of Ozone Production Sensitivity,
887 *ACS Environ. Au*, 3, 18–23, <https://doi.org/10.1021/acsenvironau.2c00048>, 2023a.
- 888 Liu, X., Yi, G., Zhou, X., Zhang, T., Bie, X., Li, J., and Tan, H.: Spatio-temporal variations of
889 PM_{2.5} and O₃ in China during 2013–2021: Impact factor analysis, *Environmental Pollution*,
890 334, 122189, <https://doi.org/10.1016/j.envpol.2023.122189>, 2023b.
- 891 Lu, Y., Kong, L., Shen, J., Liu, B., An, Y., Wang, Y., Tan, J., and Wang, L.: Characteristics and



- 892 influencing factors of ambient ozone pollution in Hangzhou in the relative humidity range
893 with high ozone levels, *Atmospheric Pollution Research*, 16, 102648,
894 <https://doi.org/10.1016/j.apr.2025.102648>, 2025.
- 895 Lyu, Y., Xu, H., Wu, H., Han, F., Lv, F., Kang, A., and Pang, X.: Spatiotemporal variations of
896 PM_{2.5} and ozone in urban agglomerations of China and meteorological drivers for ozone
897 using explainable machine learning, *Environmental Pollution*, 365, 125380,
898 <https://doi.org/10.1016/j.envpol.2024.125380>, 2025.
- 899 Meng, F., Qin, M., Tang, K., Duan, J., Fang, W., Liang, S., Ye, K., Xie, P., Sun, Y., Xie, C., Ye,
900 C., Fu, P., Liu, J., and Liu, W.: High-resolution vertical distribution and sources of HONO
901 and NO₂ in the nocturnal boundary layer in urban Beijing, China, *Atmospheric Chemistry
902 and Physics*, 20, 5071–5092, <https://doi.org/10.5194/acp-20-5071-2020>, 2020.
- 903 Monks, P. S., Archibald, A. T., Colette, A., Cooper, O., Coyle, M., Derwent, R., Fowler, D.,
904 Granier, C., Law, K. S., Mills, G. E., Stevenson, D. S., Tarasova, O., Thouret, V., von
905 Schneidmesser, E., Sommariva, R., Wild, O., and Williams, M. L.: Tropospheric ozone and
906 its precursors from the urban to the global scale from air quality to short-lived climate forcer,
907 *Atmospheric Chemistry and Physics*, 15, 8889–8973, [https://doi.org/10.5194/acp-15-8889-
908 2015](https://doi.org/10.5194/acp-15-8889-2015), 2015.
- 909 Orphal, J. and Chance, K.: Ultraviolet and visible absorption cross-sections for HITRAN, *Journal
910 of Quantitative Spectroscopy and Radiative Transfer*, 82, 491–504,
911 [https://doi.org/10.1016/S0022-4073\(03\)00173-0](https://doi.org/10.1016/S0022-4073(03)00173-0), 2003.
- 912 Park, S., Son, S.-W., Jung, M.-I., Park, J., and Park, S. S.: Evaluation of tropospheric ozone
913 reanalyses with independent ozonesonde observations in East Asia, *Geosci. Lett.*, 7, 12,
914 <https://doi.org/10.1186/s40562-020-00161-9>, 2020.
- 915 Qiao, X., Guo, H., Wang, P., Tang, Y., Ying, Q., Zhao, X., Deng, W., and Zhang, H.: Fine
916 Particulate Matter and Ozone Pollution in the 18 Cities of the Sichuan Basin in Southwestern
917 China: Model Performance and Characteristics, *Aerosol Air Qual. Res.*, 19, 2308–2319,
918 <https://doi.org/10.4209/aaqr.2019.05.0235>, 2019.
- 919 Qiu, Y., Li, X., Chai, W., Liu, Y., Song, M., Tian, X., Zou, Q., Lou, W., Zhang, W., Li, J., and
920 Zhang, Y.: Insights into ozone pollution control in urban areas by decoupling meteorological
921 factors based on machine learning, *Atmospheric Chemistry and Physics*, 25, 1749–1763,
922 <https://doi.org/10.5194/acp-25-1749-2025>, 2025.
- 923 Qu, H., Wang, Y., Zhang, R., and Li, J.: Extending Ozone-Precursor Relationships in China From
924 Peak Concentration to Peak Time, *Journal of Geophysical Research: Atmospheres*, 125,
925 e2020JD033670, <https://doi.org/10.1029/2020JD033670>, 2020.
- 926 R.Crilly, L., Kramer, L., D. Pope, F., K. Whalley, L., R. Cryer, D., E. Heard, D., D. Lee, J., Reed,
927 C., and J. Bloss, W.: On the interpretation of in situ HONO observations via photochemical
928 steady state, *Faraday Discussions*, 189, 191–212, <https://doi.org/10.1039/C5FD00224A>, 2016.
- 929 Ryan, R. G., Rhodes, S., Tully, M., Wilson, S., Jones, N., Frieß, U., and Schofield, R.: Daytime
930 HONO, NO₂ and aerosol distributions from MAX-DOAS observations in Melbourne,
931 *Atmospheric Chemistry and Physics*, 18, 13969–13985, [https://doi.org/10.5194/acp-18-
932 13969-2018](https://doi.org/10.5194/acp-18-13969-2018), 2018.
- 933 Sekiya, T., Emili, E., Miyazaki, K., Inness, A., Qu, Z., Pierce, R. B., Jones, D., Worden, H.,



- 934 Cheng, W. Y. Y., Huijnen, V., and Koren, G.: Assessing the relative impacts of satellite
935 ozone and its precursor observations to improve global tropospheric ozone analysis using
936 multiple chemical reanalysis systems, *Atmospheric Chemistry and Physics*, 25, 2243–2268,
937 <https://doi.org/10.5194/acp-25-2243-2025>, 2025.
- 938 Serdyuchenko, A., Gorshelev, V., Weber, M., Chehade, W., and Burrows, J. P.: High spectral
939 resolution ozone absorption cross-sections – Part 2: Temperature dependence,
940 *Atmospheric Measurement Techniques*, 7, 625–636, <https://doi.org/10.5194/amt-7-625-2014>,
941 2014.
- 942 Sharma, B. R., Kuttippurath, J., and Gopikrishnan, G. S.: Tropospheric ozone as an atmospheric
943 pollutant and short-lived climate forcer in the Third Pole, *Chemosphere*, 380, 144474,
944 <https://doi.org/10.1016/j.chemosphere.2025.144474>, 2025.
- 945 Shi, Y., Zeng, Q., Liu, L., Huo, J., Zhang, Z., Ding, W., and Hu, F.: Observed Evidence That
946 Subsidence Process Stabilizes the Boundary Layer and Increases the Ground Concentration
947 of Secondary Pollutants, *Journal of Geophysical Research: Atmospheres*, 127,
948 e2021JD035244, <https://doi.org/10.1029/2021JD035244>, 2022.
- 949 Shu, Z., Zhao, T., Chen, Y., Liu, Y., Yang, F., Jiang, Y., He, G., Yang, Q., and Zhang, Y.: Terrain
950 effect on atmospheric process in seasonal ozone variation over the Sichuan Basin, Southwest
951 China, *Environmental Pollution*, 338, 122622, <https://doi.org/10.1016/j.envpol.2023.122622>,
952 2023.
- 953 Song, M., Zhao, X., Liu, P., Mu, J., He, G., Zhang, C., Tong, S., Xue, C., Zhao, X., Ge, M., and
954 Mu, Y.: Atmospheric NO_x oxidation as major sources for nitrous acid (HONO), *npj Clim
955 Atmos Sci*, 6, 30, <https://doi.org/10.1038/s41612-023-00357-8>, 2023a.
- 956 Song, X., Li, X.-B., Yuan, B., He, X., Chen, Y., Wang, S., Huangfu, Y., Peng, Y., Zhang, C., Liu,
957 A., Yang, H., Liu, C., Li, J., and Shao, M.: Elucidating key factors in regulating budgets of
958 ozone and its precursors in atmospheric boundary layer, *npj Clim Atmos Sci*, 7, 262,
959 <https://doi.org/10.1038/s41612-024-00818-8>, 2024.
- 960 Song, Y., Xing, C., Liu, C., Lin, J., Wu, H., Liu, T., Lin, H., Zhang, C., Tan, W., Ji, X., Liu, H.,
961 and Li, Q.: Evaluation of transport processes over North China Plain and Yangtze River
962 Delta using MAX-DOAS observations, *Atmospheric Chemistry and Physics*, 23, 1803–1824,
963 <https://doi.org/10.5194/acp-23-1803-2023>, 2023b.
- 964 Song, Y., Wang, P., Yang, Y., Tang, J., and Liao, H.: Meteorological conditions and
965 physicochemical processes amplifying ozone pollution during heatwaves in major city
966 clusters of China, *Atmospheric Research*, 330, 108580,
967 <https://doi.org/10.1016/j.atmosres.2025.108580>, 2026.
- 968 Spataro, F. and Ianniello, A.: Sources of atmospheric nitrous acid: State of the science, current
969 research needs, and future prospects, *Journal of the Air & Waste Management Association*,
970 64, 1232–1250, <https://doi.org/10.1080/10962247.2014.952846>, 2014.
- 971 Spurr, R. J. D.: VLIDORT: A linearized pseudo-spherical vector discrete ordinate radiative
972 transfer code for forward model and retrieval studies in multilayer multiple scattering media,
973 *Journal of Quantitative Spectroscopy and Radiative Transfer*, 102, 316–342,
974 <https://doi.org/10.1016/j.jqsrt.2006.05.005>, 2006.
- 975 Stutz, J., Kim, E. S., Platt, U., Bruno, P., Perrino, C., and Febo, A.: UV-visible absorption cross



- 976 sections of nitrous acid, *Journal of Geophysical Research: Atmospheres*, 105, 14585–14592,
977 <https://doi.org/10.1029/2000JD900003>, 2000.
- 978 Su, W., Liu, C., Hu, Q., Fan, G., Xie, Z., Huang, X., Zhang, T., Chen, Z., Dong, Y., Ji, X., Liu, H.,
979 Wang, Z., and Liu, J.: Characterization of ozone in the lower troposphere during the 2016
980 G20 conference in Hangzhou, *Sci Rep*, 7, 17368, <https://doi.org/10.1038/s41598-017-17646->
981 [x](https://doi.org/10.1038/s41598-017-17646-x), 2017.
- 982 Tang, Y., An, J., Wang, F., Li, Y., Qu, Y., Chen, Y., and Lin, J.: Impacts of an unknown daytime
983 HONO source on the mixing ratio and budget of HONO, and hydroxyl, hydroperoxyl, and
984 organic peroxy radicals, in the coastal regions of China, *Atmospheric Chemistry and Physics*,
985 15, 9381–9398, <https://doi.org/10.5194/acp-15-9381-2015>, 2015.
- 986 Thalman, R. and Volkamer, R.: Temperature dependent absorption cross-sections of O₂–O₂
987 collision pairs between 340 and 630 nm and at atmospherically relevant pressure, *Phys.*
988 *Chem. Chem. Phys.*, 15, 15371, <https://doi.org/10.1039/c3cp50968k>, 2013.
- 989 Thürkow, M., Schaap, M., Kranenburg, R., Pfäfflin, F., Neunhäuserer, L., Wolke, R., Heinold, B.,
990 Stoll, J., Lupașcu, A., Nordmann, S., Minkos, A., and Butler, T.: Dynamic evaluation of
991 modeled ozone concentrations in Germany with four chemistry transport models, *Science of*
992 *The Total Environment*, 906, 167665, <https://doi.org/10.1016/j.scitotenv.2023.167665>, 2024.
- 993 Torres, O., Jethva, H., Ahn, C., Jaross, G., and Loyola, D. G.: TROPOMI aerosol products:
994 evaluation and observations of synoptic-scale carbonaceous aerosol plumes during 2018–
995 2020, *Atmospheric Measurement Techniques*, 13, 6789–6806, <https://doi.org/10.5194/amt->
996 [13-6789-2020](https://doi.org/10.5194/amt-13-6789-2020), 2020b.
- 997 Vandaele, A. C., Hermans, C., Simon, P. C., Carleer, M., Colin, R., Fally, S., Mérienne, M. F.,
998 Jenouvrier, A., and Coquart, B.: Measurements of the NO₂ absorption cross-section from 42
999 000 cm⁻¹ to 10 000 cm⁻¹ (238–1000 nm) at 220 K and 294 K, *Journal of Quantitative*
1000 *Spectroscopy and Radiative Transfer*, 59, 171–184, <https://doi.org/10.1016/S0022->
1001 [4073\(97\)00168-4](https://doi.org/10.1016/S0022-4073(97)00168-4), 1998.
- 1002 Wang, N., Du, Y., Chen, D., Meng, H., Chen, X., Zhou, L., Shi, G., Zhan, Y., Feng, M., Li, W.,
1003 Chen, M., Li, Z., and Yang, F.: Spatial disparities of ozone pollution in the Sichuan Basin
1004 spurred by extreme, hot weather, *Atmospheric Chemistry and Physics*, 24, 3029–3042,
1005 <https://doi.org/10.5194/acp-24-3029-2024>, 2024a.
- 1006 Wang, R., Shen, H., Zeng, C., Chen, J., Wang, Y., and Li, Y.: A global land daily 10-km-
1007 resolution surface ozone dataset from 2013–2022, *Sci Data*, 12, 1710,
1008 <https://doi.org/10.1038/s41597-025-05990-x>, 2025a.
- 1009 Wang, W.N., Cheng, T.H., Gu, X.F., Chen, H., Guo, H., Wang, Y., Bao, F.W., Shi, S.Y., Xu, B.R.,
1010 Zuo, X., Meng, C., and Zhang, X.C.: Assessing Spatial and Temporal Patterns of Observed
1011 Ground-level Ozone in China, *Sci Rep*, 7, 3651, <https://doi.org/10.1038/s41598-017-03929-w>,
1012 2017.
- 1013 Wang, X., Zhang, H., Hong, X., Xiang, Y., Wang, S., Zhang, T., Qin, Z., and Ou, J.: Vertical
1014 profiles and regional transport of ozone in typical area of Yangtze-Huaihe River Basin during
1015 the autumn base on multiple lidars, *Atmospheric Pollution Research*, 15, 101983,
1016 <https://doi.org/10.1016/j.apr.2023.101983>, 2024b.
- 1017 Wang, Y., Puķite, J., Wagner, T., Donner, S., Beirle, S., Hilboll, A., Vrekoussis, M., Richter, A.,



- 1018 Apituley, A., Pitters, A., Allaart, M., Eskes, H., Frumau, A., Van Roozendael, M., Lampel, J.,
1019 Platt, U., Schmitt, S., Swart, D., and Vonk, J.: Vertical Profiles of Tropospheric Ozone From
1020 MAX-DOAS Measurements During the CINDI-2 Campaign: Part 1—Development of a New
1021 Retrieval Algorithm, *Journal of Geophysical Research: Atmospheres*, 123, 10,637–10,670,
1022 <https://doi.org/10.1029/2018JD028647>, 2018.
- 1023 Wang, Y., Dörner, S., Donner, S., Böhnke, S., De Smedt, I., Dickerson, R. R., Dong, Z., He, H.,
1024 Li, Z., Li, Z., Li, D., Liu, D., Ren, X., Theys, N., Wang, Y., Wang, Y., Wang, Z., Xu, H., Xu,
1025 J., and Wagner, T.: Vertical profiles of NO₂, SO₂, HONO, HCHO, CHOCHO and aerosols
1026 derived from MAX-DOAS measurements at a rural site in the central western North China
1027 Plain and their relation to emission sources and effects of regional transport, *Atmospheric
1028 Chemistry and Physics*, 19, 5417–5449, <https://doi.org/10.5194/acp-19-5417-2019>, 2019.
- 1029 Wang, Y., Gao, W., Wang, S., Song, T., Gong, Z., Ji, D., Wang, L., Liu, Z., Tang, G., Huo, Y.,
1030 Tian, S., Li, J., Li, M., Yang, Y., Chu, B., Petäjä, T., Kerminen, V.-M., He, H., Hao, J.,
1031 Kulmala, M., Wang, Y., and Zhang, Y.: Contrasting trends of PM_{2.5} and surface-ozone
1032 concentrations in China from 2013 to 2017, *Natl Sci Rev*, 7, 1331–1339,
1033 <https://doi.org/10.1093/nsr/nwaa032>, 2020.
- 1034 Wang, Y., Yang, Y., Yuan, Q., Li, T., Zhou, Y., Zong, L., Wang, M., Xie, Z., Ho, H. C., Gao, M.,
1035 Tong, S., Lolli, S., and Zhang, L.: Substantially underestimated global health risks of current
1036 ozone pollution, *Nat Commun*, 16, 102, <https://doi.org/10.1038/s41467-024-55450-0>, 2025b.
- 1037 Wang, Z., Zhang, H., Shi, C., Ji, X., Zhu, Y., Xia, C., Sun, X., Zhang, M., Lin, X., Yan, S., Zhou,
1038 Y., Xing, C., Chen, Y., and Liu, C.: Vertical and spatial differences in ozone formation
1039 sensitivities under different ozone pollution levels in eastern Chinese cities, *npj Clim Atmos
1040 Sci*, 8, 30, <https://doi.org/10.1038/s41612-024-00855-3>, 2025c.
- 1041 Xia, N., Du, E., Guo, Z., and de Vries, W.: The diurnal cycle of summer tropospheric ozone
1042 concentrations across Chinese cities: Spatial patterns and main drivers, *Environmental
1043 Pollution*, 286, 117547, <https://doi.org/10.1016/j.envpol.2021.117547>, 2021.
- 1044 Xing, C., Liu, C., Wang, S., Chan, K. L., Gao, Y., Huang, X., Su, W., Zhang, C., Dong, Y., Fan,
1045 G., Zhang, T., Chen, Z., Hu, Q., Su, H., Xie, Z., and Liu, J.: Observations of the vertical
1046 distributions of summertime atmospheric pollutants and the corresponding ozone production
1047 in Shanghai, China, *Atmospheric Chemistry and Physics*, 17, 14275–14289,
1048 <https://doi.org/10.5194/acp-17-14275-2017>, 2017.
- 1049 Xing, C., Liu, C., Wang, S., Hu, Q., Liu, H., Tan, W., Zhang, W., Li, B., and Liu, J.: A new
1050 method to determine the aerosol optical properties from multiple-wavelength O₄ absorptions
1051 by MAX-DOAS observation, *Atmospheric Measurement Techniques*, 12, 3289–3302,
1052 <https://doi.org/10.5194/amt-12-3289-2019>, 2019.
- 1053 Xing, C., Liu, C., Wu, H., Lin, J., Wang, F., Wang, S., and Gao, M.: Ground-based vertical profile
1054 observations of atmospheric composition on the Tibetan Plateau (2017–2019), *Earth System
1055 Science Data*, 13, 4897–4912, <https://doi.org/10.5194/essd-13-4897-2021>, 2021a.
- 1056 Xing, C., Liu, C., Hu, Q., Fu, Q., Wang, S., Lin, H., Zhu, Y., Wang, S., Wang, W., Javed, Z., Ji,
1057 X., and Liu, J.: Vertical distributions of wintertime atmospheric nitrogenous compounds and
1058 the corresponding OH radicals production in Leshan, southwest China, *Journal of
1059 Environmental Sciences*, 105, 44–55, <https://doi.org/10.1016/j.jes.2020.11.019>, 2021b.



- 1060 Xing, C., Liu, C., Hong, Q., Liu, H., Wu, H., Lin, J., Song, Y., Chen, Y., Liu, T., Hu, Q., Tan, W.,
1061 and Lin, H.: Vertical distributions and potential sources of wintertime atmospheric pollutants
1062 and the corresponding ozone production on the coast of Bohai Sea, *Journal of Environmental*
1063 *Management*, 319, 115721, <https://doi.org/10.1016/j.jenvman.2022.115721>, 2022.
- 1064 Xing, C., Xu, S., Song, Y., Liu, C., Liu, Y., Lu, K., Tan, W., Zhang, C., Hu, Q., Wang, S., Wu, H.,
1065 and Lin, H.: A new insight into the vertical differences in NO₂ heterogeneous reaction to
1066 produce HONO over inland and marginal seas, *Atmospheric Chemistry and Physics*, 23,
1067 5815–5834, <https://doi.org/10.5194/acp-23-5815-2023>, 2023.
- 1068 Xing, C., Liu, C., Li, Q., Wang, S., Tan, W., Zou, T., Wang, Z., and Lu, C.: Observations of
1069 HONO and its precursors between urban and its surrounding agricultural fields: The vertical
1070 transports, sources and contribution to OH, *Science of The Total Environment*, 915, 169159,
1071 <https://doi.org/10.1016/j.scitotenv.2023.169159>, 2024a.
- 1072 Xing, C., Liu, C., Ye, C., Xue, J., Wu, H., Ji, X., Ou, J., and Hu, Q.: Observations of the vertical
1073 distributions of summertime atmospheric pollutants in Nam Co: OH production and source
1074 analysis, *Atmospheric Chemistry and Physics*, 24, 10093–10112, <https://doi.org/10.5194/acp-24-10093-2024>, 2024c.
- 1076 Xu, S., Wang, S., Xia, M., Lin, H., Xing, C., Ji, X., Su, W., Tan, W., Liu, C., and Hu, Q.:
1077 Observations by Ground-Based MAX-DOAS of the Vertical Characters of Winter Pollution
1078 and the Influencing Factors of HONO Generation in Shanghai, China, *Remote Sensing*, 13,
1079 3518, <https://doi.org/10.3390/rs13173518>, 2021.
- 1080 Xuan, H., Liu, J., Zhao, Y., Cao, Q., Chen, T., Wang, Y., Liu, Z., Sun, X., Li, H., Zhang, P., Chu,
1081 B., Ma, Q., and He, H.: Relative humidity driven nocturnal HONO formation mechanism in
1082 autumn haze events of Beijing, *npj Clim Atmos Sci*, 7, 193, <https://doi.org/10.1038/s41612-024-00745-8>, 2024.
- 1084 Xuan, H., Lian, C., Ma, P., Lan, L., Wang, W., Liu, C., Quan, J., Zhang, S., Liu, J., Li, H., Chen,
1085 T., Zhang, P., Wang, Y., Chu, B., Ma, Q., and He, H.: Vertical Distribution of Sources and
1086 Atmospheric Impacts of HONO in the North China Plain, *Environ. Sci. Technol.*, 59, 17666–
1087 17676, <https://doi.org/10.1021/acs.est.5c01801>, 2025b.
- 1088 Xue, C., Chen, H., McGillen, M. R., Su, H., Cheng, Y., Kleffmann, J., Li, G., Cazaunau, M.,
1089 Colomb, A., Sciare, J., DeWitt, L., Marchand, N., Sarda-Estevé, R., Petit, J.-E., and Kukui,
1090 A.: Role of Heterogeneous Reactions in the Atmospheric Oxidizing Capacity in Island
1091 Environments, *Environ. Sci. Technol.*, 59, 3153–3164,
1092 <https://doi.org/10.1021/acs.est.4c11647>, 2025.
- 1093 Yang, G., Liu, Y., and Li, X.: Spatiotemporal distribution of ground-level ozone in China at a city
1094 level, *Sci Rep*, 10, 7229, <https://doi.org/10.1038/s41598-020-64111-3>, 2020.
- 1095 Ye, C., Lu, K., Ma, X., Qiu, W., Li, S., Yang, X., Xue, C., Zhai, T., Liu, Y., Li, X., Li, Y., Wang,
1096 H., Tan, Z., Chen, X., Dong, H., Zeng, L., Hu, M., and Zhang, Y.: HONO chemistry at a
1097 suburban site during the EXPLORE-YRD campaign in 2018: formation mechanisms and
1098 impacts on O₃ production, *Atmospheric Chemistry and Physics*, 23, 15455–15472,
1099 <https://doi.org/10.5194/acp-23-15455-2023>, 2023.
- 1100 Yu, H., De Smedt, I., Theys, N., Snee, M., Veeffkind, P., and Van Roozendaal, M.: Harmonized
1101 cloud datasets for the Ozone Monitoring Instrument (OMI) and TROPOspheric Monitoring



- 1102 Instrument (TROPOMI) using the O₂-O₂ 477 nm absorption band, *Atmospheric*
1103 *Measurement Techniques*, 18, 4131–4163, <https://doi.org/10.5194/amt-18-4131-2025>, 2025.
- 1104 Yu, Y., Cheng, P., Li, H., Yang, W., Han, B., Song, W., Hu, W., Wang, X., Yuan, B., Shao, M.,
1105 Huang, Z., Li, Z., Zheng, J., Wang, H., and Yu, X.: Budget of nitrous acid (HONO) at an
1106 urban site in the fall season of Guangzhou, China, *Atmospheric Chemistry and Physics*, 22,
1107 8951–8971, <https://doi.org/10.5194/acp-22-8951-2022>, 2022.
- 1108 Zeng, Y., Zhang, J., Li, D., Liao, Z., Bian, J., Bai, Z., Shi, H., Xuan, Y., Yao, Z., and Chen, H.:
1109 Vertical distribution of tropospheric ozone and its sources of precursors over Beijing: Results
1110 from ~ 20 years of ozonesonde measurements based on clustering analysis, *Atmospheric*
1111 *Research*, 284, 106610, <https://doi.org/10.1016/j.atmosres.2023.106610>, 2023.
- 1112 Zhang, H., Ren, C., Zhou, X., Tang, K., Liu, Y., Liu, T., Wang, J., Chi, X., Li, M., Li, N., Huang,
1113 X., and Ding, A.: Improving HONO Simulations and Evaluating Its Impacts on Secondary
1114 Pollution in the Yangtze River Delta Region, China, *Journal of Geophysical Research:*
1115 *Atmospheres*, 129, e2024JD041052, <https://doi.org/10.1029/2024JD041052>, 2024.
- 1116 Zhang, H., Shi, C., Ying, C., Weng, S., Ni, E., Zhao, L., Yang, P., Tang, K., Zhou, X., Ren, C.,
1117 Chi, X., Zhou, D., Li, M., Li, N., Liu, T., and Huang, X.: HONO formation mechanisms and
1118 impacts on ambient oxidants in coastal regions of Fujian, China, *Atmospheric Chemistry and*
1119 *Physics*, 25, 16797–16816, <https://doi.org/10.5194/acp-25-16797-2025>, 2025a.
- 1120 Zhang, Q., Liu, P., Wang, Y., George, C., Chen, T., Ma, S., Ren, Y., Mu, Y., Song, M., Herrmann,
1121 H., Mellouki, A., Chen, J., Yue, Y., Zhao, X., Wang, S., and Zeng, Y.: Unveiling the
1122 underestimated direct emissions of nitrous acid (HONO), *Proc Natl Acad Sci U S A*, 120,
1123 e2302048120, <https://doi.org/10.1073/pnas.2302048120>, 2023a.
- 1124 Zhang, X., Tong, S., Jia, C., Zhang, W., Wang, Z., Tang, G., Hu, B., Liu, Z., Wang, L., Zhao, P.,
1125 Pan, Y., and Ge, M.: Elucidating HONO formation mechanism and its essential contribution
1126 to OH during haze events, *npj Clim Atmos Sci*, 6, 55, [https://doi.org/10.1038/s41612-023-](https://doi.org/10.1038/s41612-023-00371-w)
1127 00371-w, 2023b.
- 1128 Zhang, X., Yan, Y., Zhang, N., Wang, W., Suo, H., Jian, X., Wang, C., Ma, H., Gao, H., Yang, Z.,
1129 Huang, T., and Ma, J.: The 21st-century wetting inhibits growing surface ozone in
1130 Northwestern China, *Atmospheric Chemistry and Physics*, 25, 9669–9684,
1131 <https://doi.org/10.5194/acp-25-9669-2025>, 2025b.
- 1132 Zhang, Y., Zhang, Y., Liu, Z., Bi, S., and Zheng, Y.: Analysis of Vertical Distribution Changes
1133 and Influencing Factors of Tropospheric Ozone in China from 2005 to 2020 Based on Multi-
1134 Source Data, *International Journal of Environmental Research and Public Health*, 19, 12653,
1135 <https://doi.org/10.3390/ijerph191912653>, 2022.
- 1136 Zhou, M., Li, Y., and Zhang, F.: Spatiotemporal Variation in Ground Level Ozone and Its Driving
1137 Factors: A Comparative Study of Coastal and Inland Cities in Eastern China, *International*
1138 *Journal of Environmental Research and Public Health*, 19, 9687,
1139 <https://doi.org/10.3390/ijerph19159687>, 2022.
- 1140 Zhu, L., Wang, J., Xu, Y., Ma, N., Song, X., Qin, J., Li, B., Tsui, W. B. C., Lv, L., and Zhang, T.:
1141 Vertical Characteristics of an Ozone Pollution Episode in Hong Kong Under the Typhoon
1142 Mawar—A Case Study, *Remote Sensing*, 17, 3904, <https://doi.org/10.3390/rs17233904>,
1143 2025a.



- 1144 Zhu, X., Wang, H., Han, Y., Zhang, D., Liu, S., Zhang, Z., and Liu, Y.: Reconstructing the VOC–
1145 Ozone Research Framework Through a Systematic Review of Observation and Modeling,
1146 Sustainability, 17, 7512, <https://doi.org/10.3390/su17167512>, 2025b.
- 1147 Zou, T., Xing, C., Xue, J., Li, Q., Tan, W., Wu, Z., and Liu, C.: Transport characteristics of urban
1148 and rural aerosols based on vertical observations and deep learning predictions, Atmospheric
1149 Research, 315, 107876, <https://doi.org/10.1016/j.atmosres.2024.107876>, 2025.
- 1150 Zou, T., Xing, C., Ji, X., Tan W., Liu, C., Liu, H.: A dataset of vertical profiles of O₃, HONO and
1151 their contribution to OH radical from the hyperspectral vertical remote sensing network in China
1152 (2021-2024), Zenodo [data set], <https://doi.org/10.5281/zenodo.18489836>.